

Cite this: *J. Mater. Chem. B*,  
2024, 12, 2691

## MOF magic: zirconium-based frameworks in theranostic and bio-imaging applications

Dinesh K. Gupta,<sup>a</sup> Santosh Kumar<sup>b</sup> and Mohmmad Younus Wani<sup>c</sup>

Over the past two decades, metal–organic frameworks (MOFs) have garnered substantial scientific interest across diverse fields, spanning gas storage, catalysis, biotechnology, and more. Zirconium, abundant in nature and biologically relevant, offers an appealing combination of high content and low toxicity. Consequently, Zr-based MOFs have emerged as promising materials with significant potential in biomedical applications. These MOFs serve as effective nanocarriers for controlled drug delivery, particularly for challenging antitumor and retroviral drugs in cancer and AIDS treatment. Additionally, they exhibit prowess in bio-imaging applications. Beyond drug delivery, Zr-MOFs are notable for their mechanical, thermal, and chemical stability, making them increasingly relevant in engineering. The rising demand for stable, non-toxic Zr-MOFs facilitating facile nanoparticle formation, especially in drug delivery and imaging, is noteworthy. This review focuses on biocompatible zirconium-based metal–organic frameworks (Zr-MOFs) for controlled delivery in treating diseases like cancer and AIDS. These MOFs play a key role in theranostic approaches, integrating diagnostics and therapy. Additionally, their utility in bio-imaging underscores their versatility in advancing medical applications.

Received 29th October 2023,  
Accepted 8th February 2024

DOI: 10.1039/d3tb02562d

rsc.li/materials-b

### 1. Introduction

Metal–organic frameworks (MOFs) have become increasingly popular in various applications, ranging from gas storage, purification, separation, catalysis, nonlinear optics, magnetism, to biotechnology.<sup>1–5</sup> These versatile materials have demonstrated their potential as drug delivery vehicles, joining the ranks of other nanocarriers such as nanoparticles,<sup>6–8</sup> nanoemulsions,<sup>9</sup> hydrogels,<sup>10</sup> micelles,<sup>11,12</sup> and liposomes.<sup>13,14</sup> The need for drug carriers arises due to limitations associated with the direct delivery of conventional diagnostic and therapeutic drugs. These limitations include poor solubility, rapid clearance, inadequate pharmacokinetics, high dosage requirements, increased side effects, and non-specific targeting. Limited solubility in biological fluids is one of the key challenges encountered with conventional drugs, which hampers their effective delivery. Rapid clearance from the body further diminishes their therapeutic efficacy. Poor pharmacokinetics, which encompasses drug absorption, distribution, metabolism, and excretion, can also impede their effectiveness. Another drawback is the requirement of high dosages of conventional

drugs due to their limited specificity and targeting abilities. Inefficient drug delivery necessitates elevated drug concentrations to achieve the desired therapeutic response, often resulting in heightened side effects and potential harm to healthy tissues. To overcome these limitations, innovative drug delivery systems have been developed, including nanocarriers like Zr-based-MOFs. By encapsulating drug molecules within these carriers, various challenges associated with conventional drugs can be addressed. Nanocarriers offer advantages such as improved solubility, prolonged circulation time, controlled release, targeted delivery, reduced side effects, and enhanced pharmacokinetic profiles. While each type of nanocarrier has its own advantages and disadvantages, the overall objective remains consistent: to provide an optimal platform for drug delivery that surpasses the limitations of conventional drugs. Continued research and innovation in the field of drug delivery aim to revolutionize medical treatments, maximizing therapeutic potential and minimizing the drawbacks associated with traditional drug administration. This comprehensive review article delves into the transformative role of Zr-based MOFs, in addressing the inherent limitations ranging from poor solubility to non-specific targeting of conventional drug delivery methods, and emphasizes the critical role that Zr-based MOFs play in overcoming these hurdles. This review would serve as a valuable resource in advancing our understanding of Zr-based MOFs as an integral component in the ongoing quest for more effective and advanced frameworks for biomedical applications.

<sup>a</sup> Department of Chemistry, School of Science, U.P. Rajarshi Tandon Open University, Prayagraj-211021, UP, India<sup>b</sup> Functional Polymer Material Lab, Department of Chemistry, Harcourt Butler Technical University, Kanpur-208002, UP, India. E-mail: santoshk@hbtu.ac.in<sup>c</sup> Department of Chemistry, College of Science, University of Jeddah, 21589 Jeddah, Saudi Arabia. E-mail: mwani@uj.edu.sa

## 2. Synthesis of Zr based MOFs

The synthesis of Zr-based metal–organic frameworks (MOFs) represents a significant advancement in the field of porous materials with diverse applications. Zirconium, a robust and versatile metal node, is often employed due to its high connectivity and stability, making it an ideal candidate for constructing MOF structures. The synthesis typically involves the coordination of Zr ions with organic ligands, forming a three-dimensional network with well-defined pores. The choice of ligands plays a crucial role in dictating the properties of the framework, such as porosity and chemical reactivity. Zr-based MOFs have demonstrated exceptional performance in various applications, including gas storage, catalysis, and drug delivery. The controlled synthesis of these materials allows for tuning their properties, making them suitable for specific applications and showcasing the versatility and potential impact of Zr-based MOFs in advancing materials science and engineering.

The concepts of sustainable synthesis and Green Chemistry have made significant strides in various fields; however, their application in the context of metal–organic synthesis is still limited. Researchers are exploring green approaches, such as supercritical carbon dioxide,<sup>15</sup> microwave,<sup>16,17</sup> and solvent-assisted ligand exchange (SALE),<sup>18</sup> to activate and post-synthetically functionalize metal–organic framework (MOF) materials. These methods hold promise in assisting chemists in designing environmentally friendly and functional MOFs. Incorporating the principles of Green Chemistry into synthesis of MOFs is crucial for their successful commercialization. It requires addressing the challenges associated with synthesizing coordination metal–ligand bonds using environmentally friendly methods. The development of green and scalable synthesis routes for MOFs is still in its early stages and necessitates extensive, careful, and comparative evaluation of different synthetic techniques for each specific MOF and application. Such evaluation should consider environmental impact, toxicological aspects, and economic factors. On the other hand, computational or simulation methods<sup>19–23</sup> have emerged as valuable tools for efficiently screening hypothetical MOF structures and predicting their material properties for specific applications. The adoption of these methods by both industry and academia marks a significant development in the pursuit of implementing MOFs that are truly oriented towards environmental sustainability. To achieve the goal of sustainable MOFs, it is essential for both industry and academia to work collaboratively, emphasizing the evaluation of synthetic methods, adherence to Green Chemistry principles, and integration of computational approaches. This multidisciplinary approach holds the potential to propel the field forward and enable the realization of environmentally sustainable MOFs for diverse applications.

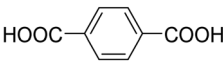
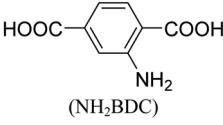
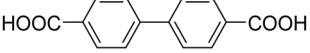
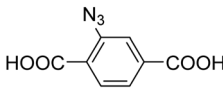
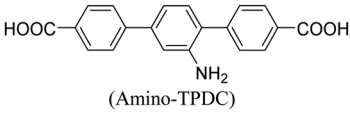
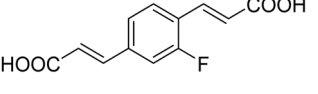
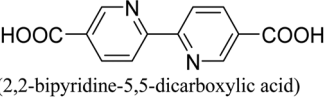
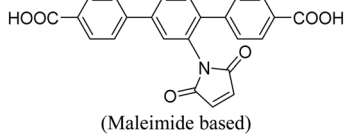
In 2008, Lillerud *et al.*<sup>24</sup> reported the discovery of clusters of  $Zr_6(\mu_3-O)_4(\mu_3-OH)_4(BDC)_6$ , commonly known as UiO-66 (UiO referring to the University of Oslo). The structure of UiO-66, characterized by 12-coordinated  $Zr_6(\mu_3-O)_4(\mu_3-OH)_4(CO_2)_{12}$ , exhibits remarkable stability, particularly under hydrothermal

conditions, surpassing the stability of most other reported metal–organic frameworks (MOFs). In 2014, Ren *et al.*<sup>25</sup> successfully synthesized Zr-based MOFs similar to UiO-66, using a microwave-assisted method. Their approach yielded highly crystalline UiO-66 with crystals taking on an octahedral shape. Notably, the synthesis reaction required only a short duration of 5 minutes. This microwave-assisted synthesis demonstrated excellent efficiency and resulted in UiO-66 structures with enhanced properties. Furthermore, the synthesized UiO-66 exhibited a hydrogen storage capacity of 1.26 wt%, showcasing its potential in applications related to hydrogen storage. In 2013, Yang *et al.* introduced a water-reflux method as a viable approach to synthesize  $Zr_6(\mu_3-O)_4(\mu_3-OH)_4(BDC-(COOH)_2)_6$ , also known as UiO-66-(COOH)<sub>2</sub>, on a relatively large scale.<sup>26</sup> Notably, this synthesis method utilized water instead of DMF (dimethylformamide), which is important considering cost-effectiveness and regeneration concerns. The incorporation of polar free carboxylic groups within the pore structure of UiO-66-(COOH)<sub>2</sub> resulted in strong interactions with CO<sub>2</sub> and exhibited high selectivity for CO<sub>2</sub>/N<sub>2</sub> adsorption. Building upon this work, Reinsch *et al.*<sup>19</sup> successfully prepared two distinct Zr-based MOFs. Firstly, they synthesized  $Zr_6(\mu_3-O)_2(\mu_3-OH)_6(BDC-F_4)_6(SO_4)$  using  $Zr(SO_4)_2$  as the metal salt and water as the solvent under mild conditions. Secondly, they synthesized  $Zr_6(\mu_3-OH)_8(OH)_2-8(SO_4)_3-6(BDC-NH_2)_3(H_2O)_{7,4}$  using the metal salt  $Zr(SO_4)_2$ , water as the solvent, and mild reaction conditions. These MOFs were obtained through controlled synthesis and exhibited unique structures and properties. The application of water as a solvent aligns with green chemistry principles, contributing to reduced environmental footprint and cost efficiencies in the synthesis of Zr-based MOFs.<sup>27</sup> Table 1 provides an overview of commonly employed synthetic and post-synthetic modification techniques for Zr-MOFs, involving a diverse range of ligands. This comprehensive examination illustrates the diverse strategies employed in the synthesis and modification of Zr-MOFs, further emphasizing their potential utility across different fields.

## 3. Structure and topology

Since the initial discovery of the UiO-66 series of metal–organic frameworks (MOFs) by Lillerud *et al.* in 2008,<sup>24</sup> which featured  $Zr_6O_4(OH)_4$  octahedral secondary building units (SBUs) connecting twelve linear dicarboxylate linkers to form a highly porous network, several other Zr-based MOFs have been characterized (Fig. 1). The majority of these MOFs are based on the Zr<sub>6</sub> SBU motif. Within Zr-based MOFs, two types of discrete Zr-based clusters have been observed. The first type is  $Zr_6O_8$  clusters, which exhibit a variety of coordination environments. The second type is  $Zr_8O_6$  clusters, which function as 12-connected nodes and have been observed in MOFs such as PCN-221. Additionally, other forms of Zr cores are found in Zr-MOFs, including single Zr(IV) ions and chain structures formed by Zr(IV) ions and ligands. Among these Zr-SBUs, the  $Zr_6(\mu_3-O)_4(\mu_3-OH)_4$  octahedral cluster is the most commonly observed. This cluster consists of six Zr(IV) centers occupying

Table 1 Summary of synthesis and post synthetic modification of Zr-MOFs

Ligand	Metal salt	MOF	Modification	Post synthetic modification	Ref.
 Terephthalic acid (Benzene-1,4-dicarboxylic acid (BDC))	ZrCl <sub>4</sub>	UiO-66	[Fe-Fe]dcbdt(CO) <sub>6</sub>	UiO-66-[Fe-Fe]dcbdt(CO) <sub>6</sub>	28
			TCAT	UiO-66-TCAT	29
			Cisplatin	UiO-66-cisplatin	13
			Taxol	UiO-66-taxol	30
			FMN	UiO-66-FMN	31
AL	AL-UiO-66				
 (NH <sub>2</sub> BDC)	ZrCl <sub>4</sub>	UiO-66-NH <sub>2</sub>	PNIPAM-NHS	UiO-66-PNIPAM	32
 Biphenyl-4,4'-dicarboxylate (BPDC)	ZrCl <sub>4</sub>	UiO-67	Cisplatin taxol		30
 (2-azido-terephthalic acid)	ZrOCl <sub>2</sub> ·8H <sub>2</sub> O	UiO-66-N <sub>3</sub>	DBCO-DNA	DNA functionalized UiO-66-Orellan	33
 (Amino-TPDC)	Zr <sup>4+</sup>	UiO	SiRNA	SiRNA/UiO-cis	34
 2-fluoro-1,4-phenylenediacrylic acid (F-H <sub>2</sub> PDA)	ZrOCl·8H <sub>2</sub> O	ZJU-800	Diclofenac sodium (DS)	DS@ZJU-800	35
 (2,2-bipyridine-5,5-dicarboxylic acid)	Zr	ZUJ-101	DS	DS@ZJU-101	35
 (Maleimide based)	ZrCl <sub>4</sub>	Mi-UiO-68	DOX and FA	DOX@UiO-68-FA	35

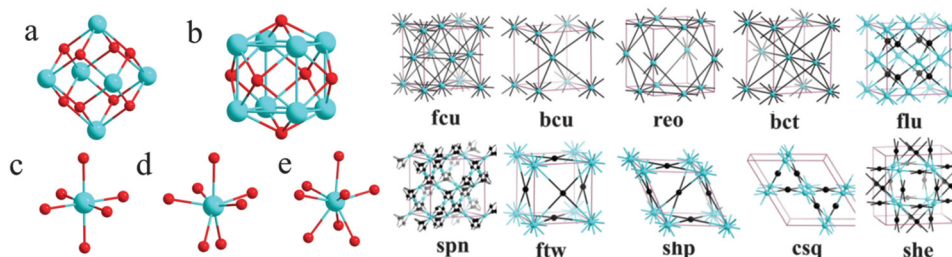
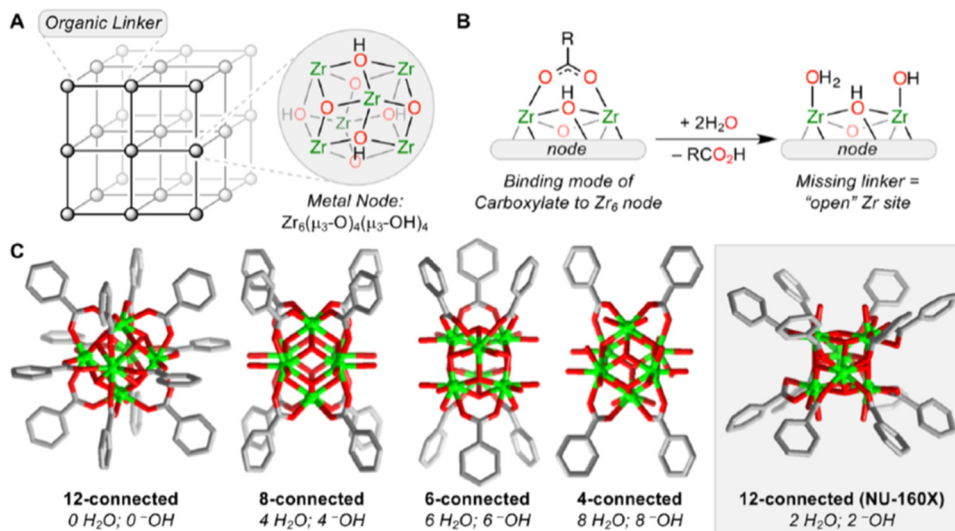


Fig. 1 Observed Zr-based clusters/cores in Zr-MOFs: (a) Zr<sub>6</sub>O<sub>8</sub> cluster, (b) Zr<sub>8</sub>O<sub>6</sub> cluster, (c) ZrO<sub>6</sub>, (d) ZrO<sub>7</sub> and (e) ZrO<sub>8</sub> and the representative network topologies in reported Zr-MOFs. Reproduced from ref. 36 with permission from American Chemical Society, Copyright 2013.

the vertices of the octahedron, with four  $\mu_3$ -OH and four  $\mu_3$ -O groups alternately capping the eight triangular faces<sup>37,38</sup> (Fig. 2 and 3). Each Zr(IV) center is eight-coordinated by oxygen atoms, exhibiting a square-antiprismatic coordination geometry.<sup>36</sup>

The discovery of UiO-66 has paved the way for the exploration of isorecticular metal-organic frameworks (MOFs).<sup>30</sup> This includes

the subsequent discovery of related MOFs such as UiO-67 (with biphenyl dicarboxylate), UiO-68 (with terphenyl dicarboxylate), and PIZOF-1 to PIZOF-8 (porous interpenetrated Zr-organic frameworks). These MOFs share a key characteristic in that they form a 12-connected network with fcu (face-centered cubic) topology. This topology influences the overall structure, including the



**Fig. 2** (A) Simplified representation of a metal–organic framework (MOF) showing metal ions or cluster nodes and ditopic organic linkers. The structure of the Zr<sub>6</sub> node in all Zr-MOFs, Zr<sub>6</sub>(μ<sub>3</sub>-O)<sub>4</sub>(μ<sub>3</sub>-OH)<sub>4</sub>, is shown here. (B) Depiction of one carboxylate ligand binding to the Zr<sub>6</sub> node, highlighting the bridging Zr–O–Zr motif. Missing carboxylate linkers, such as in missing-linker defect sites or nodes with lower connectivity, are typically replaced by one terminal aqua and one terminal hydroxo ligand. (C) Representation of the ideal node structure in 12-, 8-, 6-, and 4-connected nodes in Zr-MOFs (with the exception of NU-160X (X = 0, 1, 2), in which the 12-connected Zr<sub>6</sub> node adopts the rare hexagonal prismatic geometry). The numbers of terminal H<sub>2</sub>O and –OH ligands coordinated to the ideal node are listed below each node diagram. Reproduced from ref. 37 with permission from American Chemical Society, Copyright 2019.

shape, size, and particularly the size of the pore windows. As a result, the available pore characteristics of these MOFs are determined by the constraints imposed by the fcu topology. In UiO-type materials, access to the internal structure is regulated by triangular windows with diameters of 6, 8, and 10 Å for UiO-66, UiO-67, and UiO-68, respectively. The Zr<sub>6</sub> clusters within these MOFs consist of a Zr<sub>6</sub>O<sub>4</sub>(OH)<sub>4</sub> core, where the triangular faces of a Zr<sub>6</sub> octahedron are alternately capped by μ<sub>3</sub>-O and μ<sub>3</sub>-OH groups. Each zirconium atom is coordinated by eight oxygen atoms. This cluster core exhibits C<sub>3v</sub> symmetry, with the C<sub>3</sub> axis passing through the center of the chelated face and the triangular face opposite to it. Gomez-Gualdrón *et al.*<sup>39</sup> demonstrated that Zr-MOFs with csq, scu, or ftw topologies can be constructed using a square-shaped tetratopic ligand in combination with a Zr<sub>6</sub> cluster. Among these topologies, the Zr-MOF with ftw topology exhibits the highest surface area and the lowest propensity for structure catenation, indicating its favorable characteristics for various applications.

## 4. Biocompatibility and toxicity of Zr-MOFs

Cations such as Mg<sup>2+</sup>, Ca<sup>2+</sup>, Fe<sup>3+</sup>, and Zn<sup>2+</sup> have gained significant interest in the field of biomedical applications due to their essential roles in daily bodily functions.<sup>40,41</sup> The toxicity of a cation is closely associated with its potential accumulation within the body.<sup>42,43</sup> In contrast, certain inserted metals, like zirconium (Zr), are easily eliminated from the body, making them non-toxic and appealing for biomedical applications.<sup>44</sup>

Zirconium, widely present in nature and found in various biological systems, exhibits low toxicity.<sup>45,46</sup> Studies have

shown that zirconyl acetate, a common form of zirconium, has a lethal dose (LD<sub>50</sub>) of approximately 4.1 mg mL<sup>-1</sup> in rats. Additionally, the human body naturally contains an average of 300 mg of Zr, with a daily ingestion of about 3.5 mg per day. These factors contribute to the overall safety and biocompatibility of zirconium in biomedical applications. To provide further insight, a comprehensive study conducted by Harcojada *et al.* in 2012<sup>47</sup> summarized the toxicity and daily requirements of several metals (see Table 2). These values provide a comparative overview of the toxicity levels (measured by LD<sub>50</sub>) and daily requirements of selected metals. Notably, zirconium stands out with its low toxicity profile and minimal daily dosage, reinforcing its suitability for diverse biomedical applications.

Zirconium-based metal–organic frameworks (Zr-MOFs) have gained significant attention in chemical engineering studies due to their remarkable mechanical stability, thermostability, and chemical stability. Moreover, the pursuit of stable and non-toxic Zr-MOFs that offer simplicity in nanoparticle formation has positioned them as ideal candidates for drug delivery applications. Recently, there has been an increasing recognition of amorphous MOFs (amMOFs), which are highly disordered framework structures that retain the fundamental metal–ligand connectivity of crystalline MOFs while lacking long-range order. Ball-milling techniques have been effectively employed to trap guest molecules within these amorphous structures by irreversibly collapsing the porous networks around the occluded species. This approach introduces a novel perspective to the delivery process, as it involves not only drug diffusion through the porous network but also material degradation (such as dissolution) controlling the release. The utilization of Zr-based MOFs opens up new avenues for the

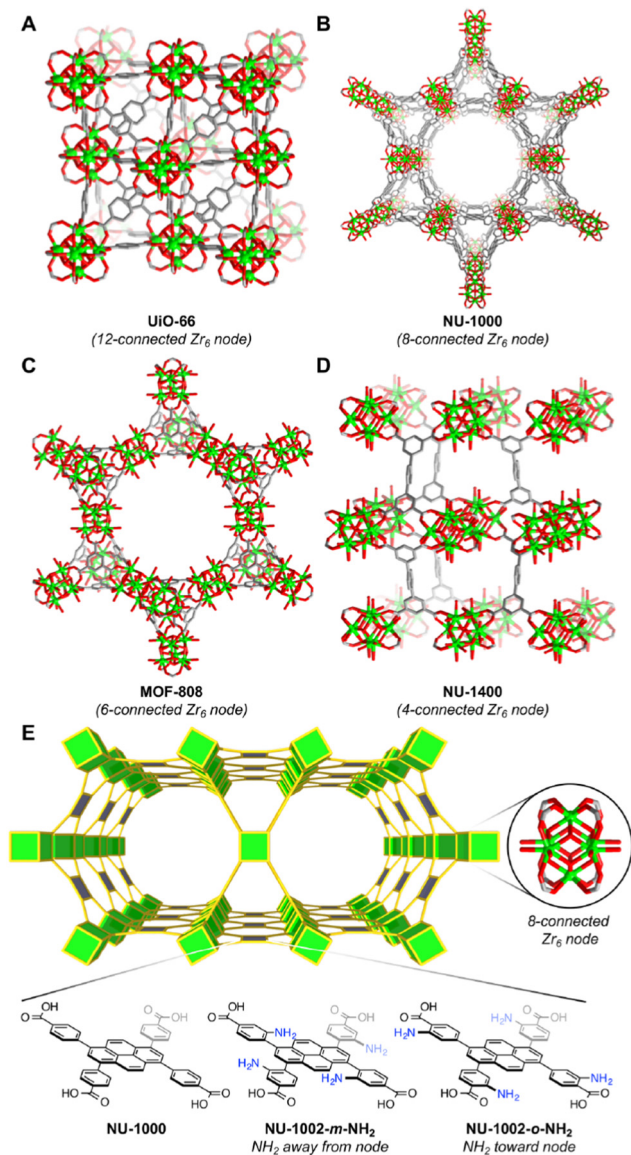


Fig. 3 Structural representations of selected Zr-MOFs with 12-, 8-, 6-, and 4-connected  $Zr_6$  nodes. (A) UiO-66 with 12-connected  $Zr_6$  nodes. Larger pore apertures can be obtained when the BDC linker in UiO-66 (A) is replaced by the  $H_4$ TBAPy linker to yield NU-1000 with 8-connected  $Zr_6$  nodes (B). (C) MOF-808 with 6-connected  $Zr_6$  nodes. (D) NU-1400 with 4-connected  $Zr_6$  nodes. (E) Illustration of Zr-MOFs based on the 4,8-connected csq net, namely, NU-1000, NU-1002-*m*-NH<sub>2</sub>, and NU-1002-*o*-NH<sub>2</sub>. The augmented net (csq-a) was used for the sake of clarity. Reproduced from ref. 38 with permission from American Chemical Society, Copyright 2020.

development of highly efficient theranostics, which encompass simultaneous therapy and diagnostics.

Zirconium-based metal-organic frameworks (Zr-MOFs) showcase immense potential in biomedical applications due to their high surface area, stability, tunability, and ability to encapsulate and deliver drugs. However, their path to clinical application hinges on a delicate balance between biocompatibility and potential toxicity. Zirconium itself is an abundant, non-toxic element present in our own bodies, and organic

Table 2 Toxicity and daily requirements of several metals

Metal	LD <sub>50</sub> (g kg <sup>-1</sup> )	Daily dose (mg)
Zirconium (Zr)	4.1	0.05
Titanium (Ti)	25	0.05
Copper (Cu)	0.025	0.8
Manganese (Mn)	1.5	5
Iron (Fe)	30	15
Zinc (Zn)	0.35	15
Magnesium (Mg)	8.1	350
Calcium (Ca)	1	1000

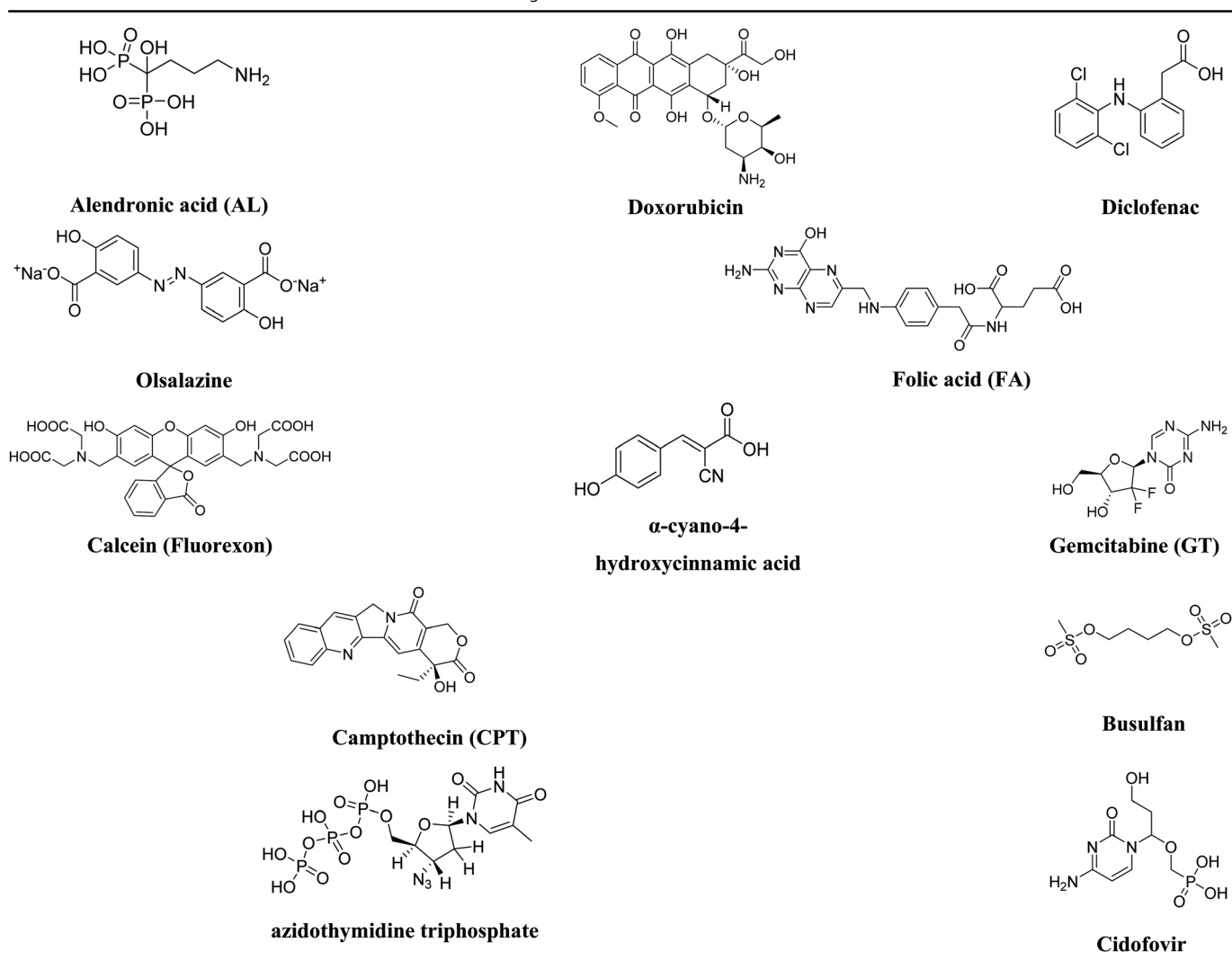
linkers in Zr-MOFs too can be carefully chosen or modified to be biocompatible and even degradable within the body. Tailoring the pore size and surface functionality would further help in minimizing cell uptake and potential immune reactions. However, challenges remain. Certain organic linkers or synthesis methods might introduce toxic impurities, demanding thorough purification and characterization. Moreover, the degradation products of Zr-MOFs need to be non-toxic and efficiently cleared by the body. Comprehensive *in vitro* and *in vivo* studies are crucial to assess the overall toxicity profile of each specific Zr-MOF in its intended application.

## 5. Zr-based MOFs in drug delivery

Drugs are chemicals that play a vital role in improving health and extending the lifespan. They are widely used as therapeutic agents, including in the treatment of severe diseases like cancer. However, drugs often come with significant drawbacks, such as poor solubility and nonselective distribution throughout the body. These issues can lead to damage to healthy tissues and cardiovascular toxicity, greatly limiting their effectiveness as therapeutic agents. One approach to overcoming these challenges is the use of drug delivery systems (DDS). These systems serve a multifaceted role in enhancing drug solubility, safeguarding drugs from degradation, enabling controlled release precisely at the target site, and mitigating toxic side effects. The quest for effective DDS in the realm of bioengineering has been an enduring challenge. In this pursuit, metal-organic frameworks (MOFs) have emerged as particularly promising candidates, owing to their distinctive characteristics. Zirconium-based metal-organic frameworks (Zr-MOFs) stand out as potent contenders for drug carriers across diverse biomedical applications, as illustrated by the array of drugs outlined in Table 3. The utilization of Zr-MOFs in drug delivery holds significant potential to revolutionize therapeutic approaches by providing tailored and efficient solutions to the complexities associated with drug administration.

Metal-organic frameworks (MOFs) showcase remarkable properties that set them apart in the realm of drug delivery.<sup>48</sup> These exceptional characteristics include their impressive pore volumes and expansive surface areas, which allow them to efficiently encapsulate and carry therapeutic payloads. Moreover, MOFs possess the unique ability to fine-tune their pore size and surface chemistry, providing an unprecedented level of control over drug release kinetics and target specificity.

Table 3 Structures of some antitumor, retroviral and other drugs



The structural diversity displayed by MOFs offers a plethora of topologies, enabling researchers to customize these materials precisely to meet the specific requirements of various drug delivery applications.<sup>49,50</sup> This versatility empowers scientists to design MOFs that can navigate through biological barriers, selectively release drugs at the desired site, and avoid premature drug degradation. The prospect of using MOFs as vehicles for drug delivery is truly captivating due to their ability to address several challenges faced by conventional drug delivery systems. By leveraging their superior characteristics, MOFs can increase drug-loading capacities, improve drug stability, and enhance the overall therapeutic efficacy. Furthermore, the biocompatibility and biodegradability of certain MOFs ensure minimal adverse effects, making them promising candidates for safe and efficient drug delivery. In recent years, researchers have been exploring the remarkable potential of zirconium-based metal-organic frameworks (Zr-MOFs) to revolutionize drug delivery systems. These MOFs possess distinctive properties, such as high pore volumes and large surface areas, which make them ideal candidates for enhancing the effectiveness of

antitumor, antiviral, and other therapeutic drugs. The versatility of Zr-MOFs allows for the encapsulation and controlled release of various therapeutic agents, enabling improved solubility and stability of drugs that might otherwise face challenges in conventional delivery methods. By entrapping different antitumor and antiviral drugs, as well as other pharmaceutical compounds, within the framework of Zr-MOFs, researchers aim to achieve targeted delivery to specific cells or tissues, thereby reducing off-target effects and increasing the therapeutic efficacy of these medications as highlighted for some selected Zr-MOFs in Table 4. Through precise engineering of Zr-MOFs, researchers can customize the pore size, surface chemistry, and drug-loading capacity to suit the specific requirements of different therapeutic agents. This fine-tuning of Zr-MOFs empowers them to serve as efficient carriers for a wide range of drugs, ensuring optimal drug release kinetics and improving patient outcomes. By delving into the realm of MOFs as drug delivery vehicles, scientists are opening up a promising avenue for advancements in the field of bioengineering. This exploration has the potential to overcome existing limitations and revolutionize drug delivery strategies, paving the

Table 4 Zr-based MOFs as drug nanocarriers with biomedical applications

MOFs	Major components	Drug/cargo	Loading percentage [wt%]	Targeted cell lines	Ref.
UiO-N <sub>3</sub> NMOF	ZrCl <sub>4</sub> , amino-TPDC	Cisplatin prodrug, siRNA	12.3 ± 1.2	Ovarian cancer cells	34
Nano-UiO-66-2-NH <sub>2</sub>	ZrCl <sub>4</sub> , 1,4-BDC_NH <sub>2</sub>	5-Fu	27	—	33
UiO-66_X	Zirconium polyhedral, 1,4-BDC_X	Caffeine	22.4 ± 3.4 (X = H) 21.2 ± 0.7 (X = Br) 13.2 ± 0.2 (X = NH <sub>2</sub> )	—	51
UiO-66	ZrCl <sub>4</sub> , 1,4-BDC	AL	51.5	MCF-7, HepG2	30
ZJU-101	Zirconium, BPYDC	Diclofenac sodium	35.3	PC12	52
PCN-221	ZrCl <sub>4</sub> , TCPP	MTX	28.6	PC12	37
UiO-66-PNIPAM	ZrCl <sub>4</sub> , 1,4-BDC_NH <sub>2</sub> , PNIPAM	Resorufin, caffeine	—	—	32
ZJU-800	ZrOCl <sub>2</sub> ·8H <sub>2</sub> O, F-H <sub>2</sub> PDA	Diclofenac sodium (DS)	58.8	PC12	53
UiO-66-NH <sub>2</sub>	ZrCl <sub>4</sub> , 1,4-BDC_NH <sub>2</sub> , CP5,	5-Fu	1.5	HEK293	54
UiO-66-NH <sub>2</sub>	ZrCl <sub>4</sub> , 1,4-BDC_NH <sub>2</sub> , CP5,	Calcein	3.1	HEK293	55
β-CD-capped	ZrCl <sub>4</sub> , 2'- <i>p</i> -tolylidiazonyl-1,1': 4,4'	RhB	—	—	56
Fe <sub>3</sub> O <sub>4</sub> @UiO-66	ZrCl <sub>4</sub> , 1,4-BDC, Fe <sub>3</sub> O <sub>4</sub>	DOX	—	HeLa cells, 3T <sub>3</sub> cells	57
UiO-PDT	ZrCl <sub>4</sub> , 1,4-BDC, I2-BDP	Photodynamic therapy	—	B16F10, C26, CT26	58
mem@catalase	Glucose oxidase (GOx)	Cancer starvation therapy	—	4T1	59
amUiO-66	Calcein, amUiO-66	Calcein	—	HeLa cell	60
α-CHC@Zr-L1 or	ZrCl <sub>4</sub> , 1,4-BDC or BPDC	α-CHC	—	HeLa cell	61
UiO-66-N <sub>3</sub>	ZrOCl <sub>2</sub> ·8H <sub>2</sub> O, 1,4-BDC_N <sub>3</sub>	DBCO-DNA oligonucleotides on surface	—	—	30
Mi-UiO-68	ZrCl <sub>4</sub> , maleimide	DOX and FA	—	—	62
NU-1000	ZrCl <sub>4</sub> , TBAPy	<i>p</i> -Cresyl sulfate	—	Human serum albumin	63
PCN-225	DSCP, PEG & silica	—	—	Optical imaging	64
PCN-94	ETTC <sup>4-</sup>	—	—	Photoluminescence	65
UiO-66@SiO <sub>2</sub>	ZrCl <sub>4</sub> :H <sub>2</sub> O	Doxorubicin	—	MCF-7 breast cancer cells	66
UiO-66-NH <sub>2</sub>	FeCl <sub>3</sub> ·6H <sub>2</sub> O	Quercetin	—	Human breast cancer cells	67

way for groundbreaking approaches to improve patient outcomes in the realm of medicine.

### 5.1. Delivery of antitumor drugs

Zr-MOFs can serve as effective carriers for various antitumor agents, safeguarding the drugs from premature degradation and facilitating controlled release at the target site.<sup>68</sup> The versatile nature of Zr-MOFs allows for the customization of their properties to optimize drug-loading capacities and release kinetics. Additionally, the biocompatibility of Zr-based materials, combined with their ability to avoid immune responses, positions them as promising vehicles for antitumor drug delivery. Current research in this domain has the capacity to transform cancer treatment strategies by leveraging the distinct advantages of Zr-metal-organic frameworks (Zr-MOFs) for delivering therapeutic agents with superior precision and efficacy. An investigative study, concentrating on the integration of cisplatin and a Pt(IV) cisplatin prodrug into two zirconium-based MOFs, UiO-66 and UiO-66-NH<sub>2</sub>, utilizing conjugation and encapsulation techniques, has yielded noteworthy outcomes.<sup>69</sup> In one approach, the Pt(IV) cisplatin prodrug was incorporated into UiO-66-NH<sub>2</sub> through an amide coupling reaction with the NH<sub>2</sub> groups. In the second approach, cisplatin was encapsulated within the spacious cavities of both MOFs. Cytotoxicity assessments conducted on the A549 lung cancer cell line revealed that the system in which cisplatin was conjugated to UiO66-NH<sub>2</sub> demonstrated greater efficiency in

inducing cell death compared to materials where cisplatin was encapsulated into the pores of the MOFs. These findings underscore the potential of integrating cisplatin and prodrugs into MOFs to enhance drug delivery in cancer treatment. The distinctive features of MOFs, such as their capacious cavities and high loading capacities, present promising opportunities for advancing the efficacy of anticancer therapies.

Fluorouracil, an extensively utilized antitumoral drug, has been commonly loaded into nano metal-organic frameworks (NMOFs). This has been substantiated by numerous examples reported to date, including a study by Yang *et al.* in 2015,<sup>62</sup> in which they described the utilization of microporous UiO-66-NH<sub>2</sub> particles for loading the drug (Fig. 4). Additionally, they employed [2]pseudorotaxanes as gatekeepers within the nanocarriers, connected through host-guest complexation to regulate the controlled release of the drug. This approach allows for precise control over the release of fluorouracil from the NMOFs, enhancing its therapeutic efficacy.

The UiO-68-azo MOF exhibits potential as a reservoir for cargo storage in water. Furthermore, the cargo-loaded MOF can be modified by capping it with β-cyclodextrin (β-CD), resulting in the creation of a mechanized MOF. In this configuration, the azobenzene trail extends from the surface of UiO-68-azo, while the bulky supramolecular complexes are positioned near the pore openings. This arrangement effectively seals the pores, preventing the spontaneous release of cargo trapped inside. Upon exposure to external chemical or physical stimuli, the

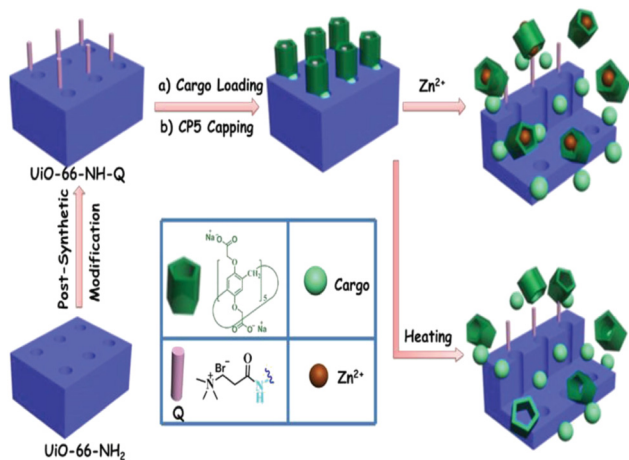


Fig. 4 Schematic representation of stimuli-responsive mechanized UiO-66-NH<sub>2</sub> MOFs equipped with positively charged quaternary ammonium salt (Q) encircled by pillarene [2]pseudorotaxanes. The mechanized nanoUiO-66-NH<sub>2</sub> MOFs can be operated either by thermal heating or by Zn<sup>2+</sup> competitive binding in regulation of the release of cargo molecules. Reproduced from ref. 62 with permission from Royal Society of Chemistry, copyright 2015.

mechanized MOF demonstrates controlled cargo release. This release is triggered by the dissociation of  $\beta$ -CD rings from the azobenzene stalks on the MOF surface. This responsive behavior allows for on-demand cargo release based on specific environmental cues. This proof-of-concept research not only presents a straightforward method for constructing stimuli-responsive mechanized MOFs but also establishes a unique MOF platform for controlled drug delivery.<sup>70</sup> The ability to selectively release cargo from the MOF in response to specific triggers holds significant promise for the development of advanced drug delivery systems.

Zirconium-based nanocrystals of a Pt(IV) cisplatin prodrug, specifically disuccinate cisplatin (DSCP), have been developed, aiming to leverage the robust Zr-carboxylate bond. The synthesis of these Zr-DSCP nanocrystals (NCPs) involves the acetone-induced precipitation of a solution containing ZrCl<sub>4</sub> and DSCP in *N,N*-dimethylformamide (DMF). The resulting particles have an average size of approximately 190 nm. Fluorescently labeled UiO-type nano metal-organic frameworks (F-UiO NMOFs) were efficiently taken up by cells and retained their structural integrity within endosomes, providing an opportunity to

monitor endosomal/lysosomal pH. Live cell imaging experiments revealed the processes of endocytosis and exocytosis of F-UiO NMOFs, as well as the acidification of endosomes over time. The study clearly demonstrated the advantages of using F-UiO NMOFs as nanosensors for real-time sensing of pH inside live cells.<sup>71</sup> These fluorescently labeled NMOFs offer a novel class of nanosensors for investigating intracellular pH dynamics and exploring interactions between NMOFs and cells.

Nanoscale coordination polymers (NCPs) have emerged as a promising platform for drug delivery due to their numerous advantages over small-molecule chemotherapeutics. These advantages include the ability to carry high payloads, lower systemic toxicity, tunability, and improved tumor uptake. However, current formulations for delivering methotrexate (MTX), an antifolate cancer drug, have limited drug loadings. A novel approach in which MTX is incorporated as a building block within an NCP formulation, resulting in remarkably high drug loadings of up to 79.1 wt%, has been reported.<sup>72</sup> This high drug loading capacity is a significant improvement compared to existing MTX delivery formulations (Fig. 5). Moreover, the developed NCP formulation demonstrated selective delivery to cancer cells, enhancing its efficacy and minimizing potential off-target effects. By utilizing MTX as a building block within NCPs, not only exceptional drug loadings but also targeted delivery to cancer cells has been achieved. These findings pave the way for the development of more efficient and specific drug delivery systems for cancer therapy, addressing the limitations of current MTX formulations and improving treatment outcomes.

A solvothermal reaction using ZrCl<sub>4</sub>, 2-azido-1,4-benzenedicarboxylic acid (N<sub>3</sub>-BDC), and 2-aminoterephthalic acid (NH<sub>2</sub>-BDC) in DMF resulted in the production of N<sub>3</sub>-UiO-66-NH<sub>2</sub> as brown powder, which upon undergoing a covalent post-synthetic method generated E-UiO-66-Pc as blue powder (Fig. 6). This involved modifying N<sub>3</sub>-UiO-66-NH<sub>2</sub> through amidation reactions and click chemistry reactions with carboxyl substituted zinc phthalocyanine and erlotinib, respectively. The Zr metal centers loaded with different ligands were denoted as Zr-L<sub>1</sub> to Zr-L<sub>6</sub>.  $\alpha$ -Cyano-4-hydroxycinnamic acid ( $\alpha$ -CHC) was used as the loaded ligand. L<sub>1</sub> represents BDC, which is used for UiO-66, while L<sub>2</sub> to L<sub>4</sub> represent BDC functionalized with -Br, -NO<sub>2</sub>, and -NH<sub>2</sub>, respectively. L<sub>5</sub> and L<sub>6</sub> correspond to extended linkers, namely naphthalene-2,6-dicarboxylic acid and 4,4'-biphenyldicarboxylic acid, respectively. The researchers

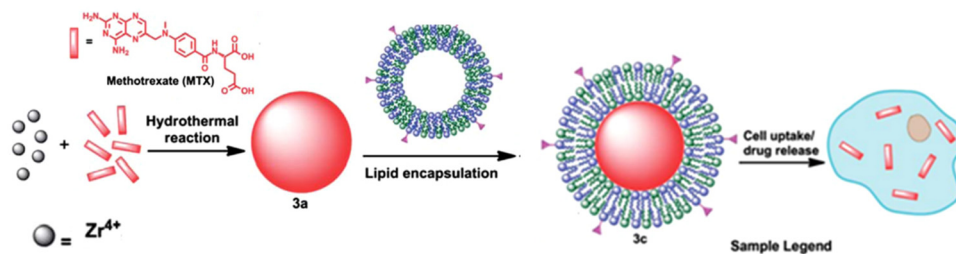
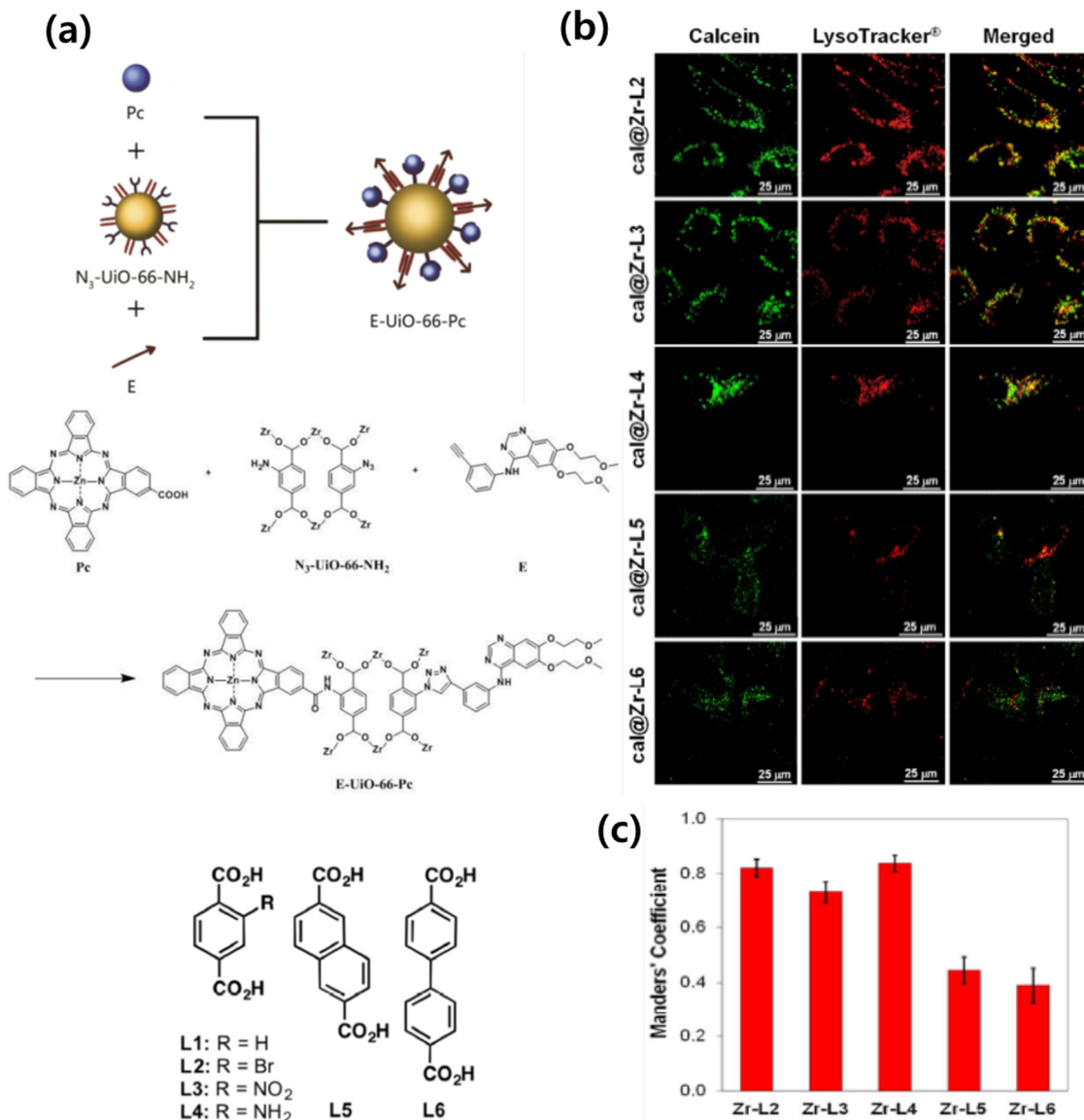


Fig. 5 Synthesis of NCPs and functionalization of MTX-containing NCPs with a lipid bilayer and targeting moiety. Reproduced from ref. 72 with permission from Royal Society of Chemistry, copyright 2012.





**Fig. 6** (a) Organic linkers used to synthesize the Zr-based MOFs. (b) Confocal microscopy images of HeLa cells incubated with Zr-based MOFs loaded with calcein (green fluorescence, i.e. calcein), and LysoTracker R-Deep red (red fluorescence), for 2 h. (c) Manders' overlapping coefficients for all the MOF samples and the lysosome marker. Error bars represent the standard error of at least 10 independent images. Reproduced from ref. 61 with permission from American Chemical Society, copyright 2017.

discovered that  $\alpha$ -CHC@Zr-L<sub>6</sub> exhibited higher toxicity compared to  $\alpha$ -CHC@Zr-L<sub>1</sub>.<sup>61</sup>

A comparison of Zr-L<sub>1</sub> and Zr-L<sub>6</sub> also confirmed that it is not necessarily the amount of drug loaded in the MOF that determines its efficacy, given that Zr-L<sub>1</sub>, which has a higher loading than Zr-L<sub>6</sub>, is still less effective at killing cells.<sup>30</sup> Release behavior of guest molecules (resorufin, caffeine, and procainamide) from UiO-66-PNIPAM was investigated in water at 25 °C and 40 °C for seven days. The release ratio was determined from the absorbance at 572 nm (resorufin), 273 nm (caffeine), and 311 nm (procainamide). A controlled release system developed by incorporating a thermoresponsive polymer, PNIPAM, onto a metal-organic framework (MOF) through a surface-selective post-synthetic modification approach was developed

(Fig. 7). This innovative MOF-PNIPAM hybrid exhibited temperature-dependent switching between “open” and “closed” states, facilitated by the conformational changes of PNIPAM grafted onto the MOF. As a result, the release of guest molecules, including resorufin, caffeine, and procainamide, was precisely regulated based on temperature variations.<sup>32,73</sup>

Spherical nucleic acid (SNA)-gold nanoparticle conjugates possess a remarkable capability to enter cells effectively, bypassing the need for cationic or viral transfection agents. These conjugates are synthesized by combining citrate-stabilized gold nanoparticles with alkythiol functionalized oligonucleotides (such as DNA or RNA). This unique property of SNAs has made them a fundamental component in intracellular diagnostic techniques, drug delivery systems, and gene

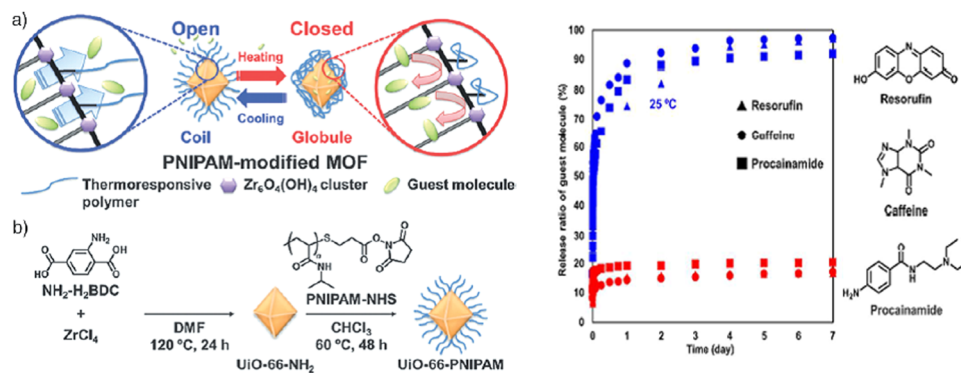


Fig. 7 (a) Schematic illustrating temperature control of pore openings in PNIPAM-modified UiO-66-NH<sub>2</sub>. (b) The post-synthetic surface modification procedure to install PNIPAM on the surface of UiO-66-NH<sub>2</sub>. Reproduced from ref. 32 with permission from Royal Society of Chemistry, copyright 2015.

regulation strategies.<sup>33</sup> Apart from their enhanced cellular uptake, SNAs also exhibit resistance to nuclease degradation, minimal cellular cytotoxicity, and low immunogenicity, which greatly enhances their suitability for various applications. In a study, the synthesis and characterization of a zirconium-based framework called UiO-66-N<sub>3</sub> (Zr<sub>6</sub>O<sub>4</sub>(OH)<sub>4</sub>(C<sub>8</sub>H<sub>3</sub>O<sub>4</sub>-N<sub>3</sub>)<sub>6</sub>) has been reported.<sup>33</sup> UiO-66-N<sub>3</sub> is a structural analogue of UiO-66 and can be readily functionalized with oligonucleotides through Cu-free strained-alkyne click chemistry (Fig. 8). This reaction has been widely employed to interface metal-organic frameworks (MOFs) with a diverse range of organic functionalities in bulk materials.

In a study conducted by Zhu *et al.*, AL-UiO-66, which refers to UiO-66 nanoparticles (NPs) acting as carriers for alendronate (AL)

delivery, was utilized.<sup>30</sup> Alendronate, an amino bisphosphonate, is commonly used in the treatment of osteoporosis, solid tumor bone metastases, myeloma bone disease, and has shown promising effects against prostate and breast cancers. However, its poor bioavailability necessitates high doses for practical clinical applications, which can potentially lead to systemic toxicity. Hence, there is a need for a continuous AL delivery system that enhances the loading capacity and delivery efficiency of AL into cancer cells. The research team achieved an unprecedented drug loading capacity by utilizing the inherent drug anchorage provided by the Zr-O clusters in UiO-66 NPs. The encapsulated AL exhibited pH-dependent release and demonstrated more efficient inhibition of cancer cell growth compared to the free drug. Approximately 42.7% of

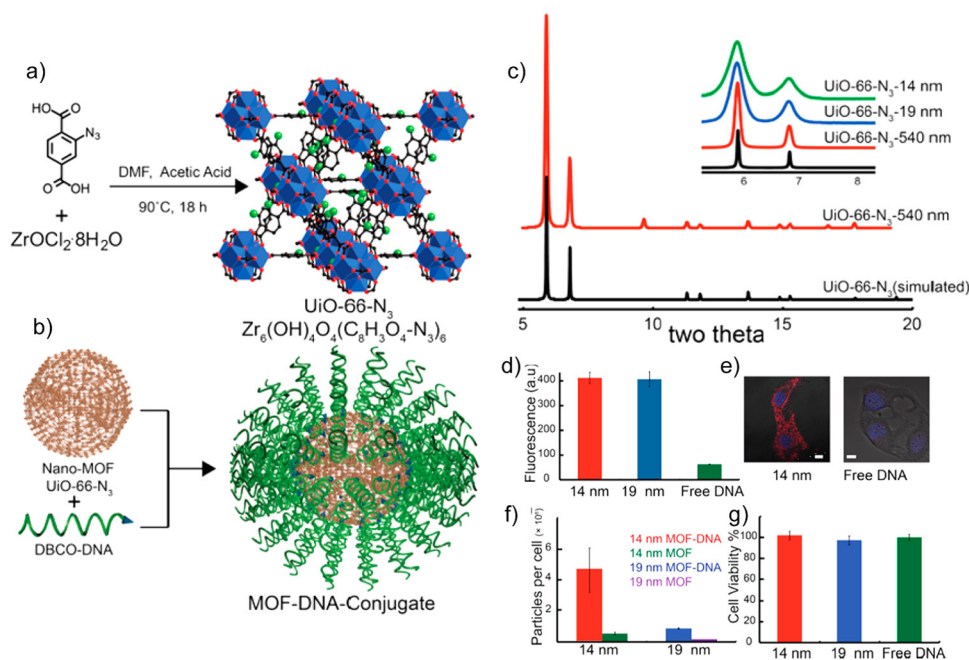


Fig. 8 (a) Synthesis of UiO-66-N<sub>3</sub> NMOFs. (b) DNA functionalization of UiO-66-N<sub>3</sub> NMOFs, utilizing DNA functionalized with dibenzylcyclooctyne. (c) Powder X-ray diffraction of simulated UiO-66-N<sub>3</sub> (black) and as-synthesized UiO-66-N<sub>3</sub> 540 nm NMOFs (red). (d) Cell uptake by flow cytometry. (e) Confocal microscopy of cells treated with 14 nm NMOF-DNA conjugates. Bar = 10 μm. (f) NMOF uptake per cell determined by ICP-MS. (g) Cell viability assay showing no significant cell toxicity for NMOF-DNA conjugates. Reproduced from ref. 33 with permission from American Chemical Society, copyright 2014.

adsorbed AL was released by UiO-66 NPs at pH 7.4. Notably, within 108 hours, the released amount reached up to 88.1% at pH 7.4, while it was less than 76% at pH 5.5. To assess the cytotoxicity of pristine UiO-66 NPs, standard MTT assays were conducted on HepG2 and MCF-7 cells to examine cell viability. The results showed negligible changes in cell viability after 24 and 48 hours of incubation. Even at a high concentration of up to  $300 \text{ mg mL}^{-1}$  of the nanocarrier, cell proliferation was only slightly hindered after 48 hours, indicating the relatively good biocompatibility of UiO-66 NPs. Furthermore, after 48 hours of incubation, AL-UiO-66 demonstrated higher cancer cell death rates compared to free AL. Interestingly, the  $\text{IC}_{50}$  values of AL-UiO-66 were significantly lower than those of free AL, indicating a higher effectiveness of AL-UiO-66 in inhibiting cancer cell growth.

A study conducted on nanoscale Zr-based metal-organic frameworks (MOFs), specifically UiO-66 and UiO-67, as potential carriers for anticancer drugs has shown promising results.<sup>74</sup> Two model drugs, hydrophobic paclitaxel and hydrophilic cisplatin, which were adsorbed onto or into the nano MOFs (NMOFs) were used. To create sustained release formulations and reduce drug toxicity, the drug-loaded MOFs were encapsulated within a modified poly( $\epsilon$ -caprolactone) with a  $D$ - $\alpha$ -tocopheryl polyethylene glycol succinate polymeric matrix, forming microparticles. The physical state of the drugs and their release rates were studied at  $37^\circ\text{C}$  using simulated body fluid. The results indicated that the drug release was influenced by the interaction between the MOFs and the drugs, while the controlled release rates were attributed to the microencapsulated formulations. *In vitro* antitumor activity was evaluated using HSC-3 (human oral squamous carcinoma; head and neck) and U-87 MG (human glioblastoma grade IV; astrocytoma) cancer cells. Cytotoxicity studies revealed that the polymer-coated, drug-loaded MOFs exhibited superior anticancer activity compared to free paclitaxel and cisplatin solutions at various concentrations.

A novel theranostic composite,  $\text{Fe}_3\text{O}_4@\text{UiO-66}$ , was developed by incorporating  $\text{Fe}_3\text{O}_4$  nanoparticles into the MOF UiO-66.<sup>57</sup> This composite demonstrated potential for both *in vitro* and *in vivo* applications in magnetic resonance (MR) imaging and drug delivery. UiO-66, a zirconium-based MOF constructed with  $\text{Zr(IV)}$  ions and  $\text{NH}_2\text{-H}_2\text{BDC}$  ligands, has garnered considerable attention in the field of drug delivery due to its exceptional chemical and solvent stability. The unique structure of UiO-66 consists of  $\text{Zr(IV)}$ -clusters and linear ligands, forming a rigid cubic porous framework with octahedral cavities (1.1 nm diameter) and tetrahedral cavities (0.6 nm diameter). The  $\text{Fe}_3\text{O}_4@\text{UiO-66}$  composites exhibited a high drug loading capacity, attributed to the large surface area of the UiO-66 shell and the interactions between the drug, specifically DOX (doxorubicin), and UiO-66. The strong interaction between DOX and  $\text{Fe}_3\text{O}_4@\text{UiO-66}$  was confirmed by the significant fluorescence quenching of DOX and a color change from brown to wine in the  $\text{Fe}_3\text{O}_4@\text{UiO-66}$ -DOX dispersion.

The release behavior of DOX from  $\text{Fe}_3\text{O}_4@\text{UiO-66}$ -DOX composites was investigated under different pH conditions (4.0, 5.0, 6.0, 7.4 and 8.0).<sup>75</sup> The cumulative drug release over time exhibited a slow and sustained pattern, without any burst release effect. This controlled release profile ensured a stable drug concentration and allowed sufficient time for  $\text{Fe}_3\text{O}_4@\text{UiO-66}$ -DOX to accumulate at the tumor site.  $\text{Fe}_3\text{O}_4@\text{UiO-66}$  also has the ability to act as a contrast agent for MR imaging.<sup>75</sup> Another study involving nano-UiO-66-2- $\text{NH}_2$  demonstrated its capability to load up to 27 wt% of 5-Fu (5-fluorouracil) and exhibited good, sustained release properties.<sup>53</sup> The calculated release rate constant ( $k$ ) was  $0.27 \text{ h}^{-1}$  in PBS solution at  $37^\circ\text{C}$ . These findings highlight the potential for developing nano-MOFs with adjustable particle sizes and functions to meet specific application requirements. This inspires further exploration into facile methods for the preparation of such nanoMOFs with tailored properties.

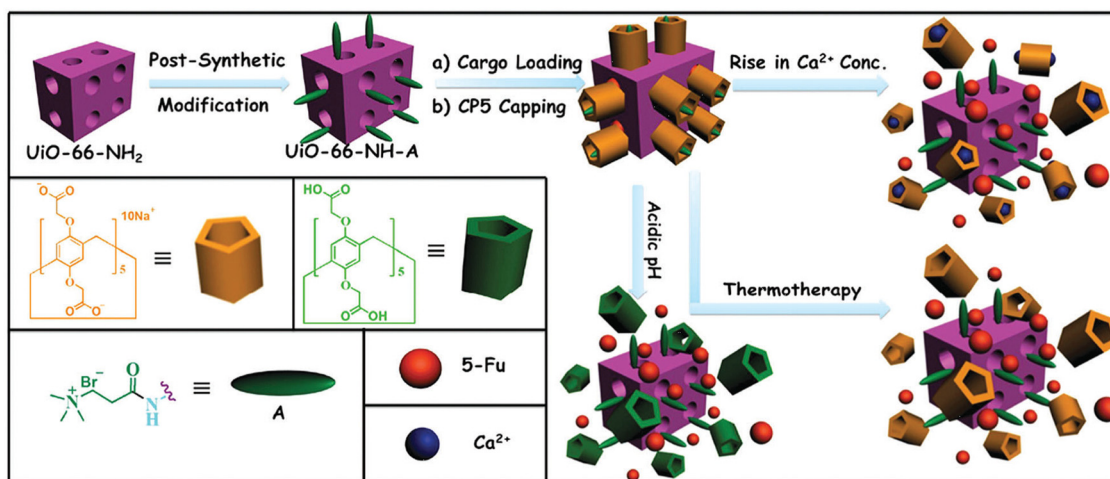


Fig. 9 Schematic representation of stimuli-responsive mechanized Zr-MOFs ( $\text{UiO-66-NH}_2$ ) with positively charged A stalks encircled by carboxylatopillar[5]arene (CP5) rings on the surfaces. The mechanized  $\text{UiO-66-NH}_2$  Zr-MOFs can be operated by pH changes,  $\text{Ca}^{2+}$  concentrations, and thermotherapy to regulate the release of 5-Fu. Reproduced from ref. 76 with permission from Royal Society of Chemistry, copyright 2016.

Multi-stimuli responsive “gated scaffolds” have been designed by combining capped metal–organic frameworks (MOFs) with supramolecular [2]pseudorotaxanes (Fig. 9). These mechanized Zr-MOFs exhibit high drug encapsulation, minimal premature release, low cytotoxicity, and good biocompatibility. The drug release is triggered by variations in pH and  $\text{Ca}^{2+}$  concentration within bone tumor cells and can also be controlled through hyperthermia.<sup>76</sup> This innovative approach holds promise for developing smart biomaterials for bone regeneration and cancer therapy.

Carboxyl-functionalized diiodo-substituted BODIPYs (I2-BDP) have been successfully incorporated into nanoscale UiO MOFs (UiO-66) using solvent-assisted ligand exchange (SALE) to create UiO-PDT.<sup>58</sup> These UiO-PDT nanocrystals have exhibited excellent biocompatibility and demonstrated highly efficient generation of singlet oxygen, which effectively killed cancer cells. Under dark conditions, B16F10 cells treated with UiO-PDT and I2-BDP remained alive and displayed a green color after one day of incubation. However, upon light irradiation, almost all of the B16F10 cells treated with UiO-PDT turned red, indicating cell death. Therefore, the synthesized UiO-PDT nanocrystals have the potential to be utilized as agents for photodynamic therapy, offering effective cancer cell eradication. BODIPY-based zirconium MOFs have been reported to show interesting results in several photodynamic therapy studies.<sup>77,78</sup>

To achieve synergistic starvation and photodynamic therapy (PDT), a cancer cell membrane-camouflaged cancer-targeted cascade bioreactor (mCGP) was constructed using porphyrin metal–organic frameworks (MOFs) of PCN-224.<sup>59</sup> This bioreactor embedded glucose oxidase (GOx) and catalase within the MOFs as shown in Fig. 10. Upon internalization by cancer cells, mCGP demonstrated the ability to promote oxygenation in the

microenvironment by catalyzing the conversion of endogenous hydrogen peroxide ( $\text{H}_2\text{O}_2$ ) to oxygen ( $\text{O}_2$ ). This process was further enhanced under light irradiation, leading to increased decomposition of intracellular glucose and enhanced production of cytotoxic singlet oxygen ( $^1\text{O}_2$ ). As a result, mCGP exhibited amplified synergistic therapeutic effects by combining long-term cancer starvation therapy with robust PDT. This approach efficiently inhibited cancer growth and allowed for spatiotemporally controlled cancer treatment.

In a study conducted by Orellana-Tavra *et al.* in 2015,<sup>55</sup> calcein, a hydrophilic molecule, was encapsulated within the Zr-based MOF UiO-66. Subsequently, the framework was amorphized using ball-milling. The researchers demonstrated that the amorphized UiO-66 exhibited controlled release of calcein for over 30 days, in contrast to the 2-day release period observed with crystalline UiO-66. Calcein was chosen as a model drug due to its structural similarities to doxorubicin, a well-known anti-cancer drug. The drug release from the pores of MOFs NU-1000 and NU-901 can be effectively delayed by a temperature treatment process.<sup>60</sup> These MOFs possess large pore volumes and sizes, allowing for exceptional loading of model drugs, with percentages exceeding 35 wt%. Specifically, the MOF NU-1000 encapsulates the anticancer drug calcein, resulting in Cal@NU-1000, while the MOF NU-901 encapsulates alphacyano-4-hydroxycinnamic acid ( $\alpha$ -CHC), leading to  $\alpha$ -CHC@NU-901. By subjecting these MOFs to subsequent temperature treatments, the drug loadings remain stable, avoiding a burst release effect. Moreover, these loaded MOFs demonstrate efficacy in killing cells, indicating their potential for therapeutic applications.

A novel, multifunctional drug delivery system for hepatoma (HepG2) therapy, named DOX@UiO-68-FA (Fig. 11), has been designed and synthesized using a nanoscale metal–organic

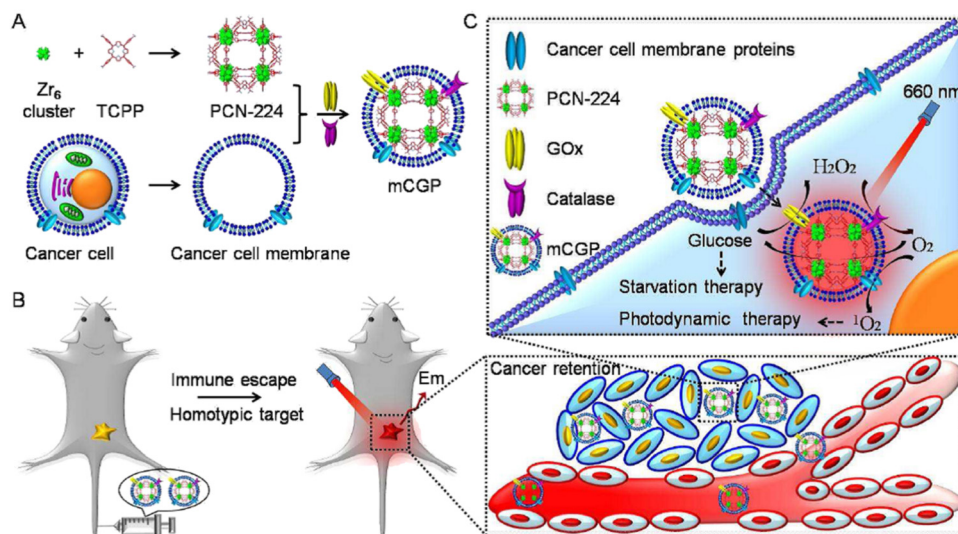


**Fig. 10** Schematic illustration of the cancer cell membrane camouflaged cascade bioreactor for cancer targeting starvation therapy and PDT. (A) The preparation processes of mCGP. (B) The immune escape and homotypic targeting abilities of mCGP endowing cancer accumulation and retention behaviors after intravenous injection. (C) The cascade reactions would amplify the synergistic effects of mCGP to cut off the cancer cell glucose supply for starvation therapy and promote the  $^1\text{O}_2$  generation for PDT under light irradiation. Reproduced from ref. 59 with permission from Royal Society of Chemistry, copyright 2016.

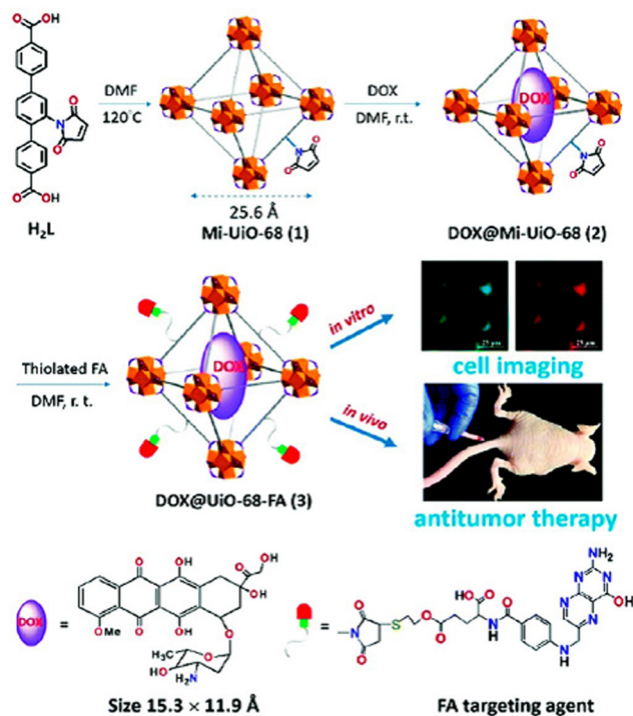


Fig. 11 Design and fabrication of a FA targeting agent decorated drug delivery system, and its application in cell imaging and *in vivo* antitumor therapy. Reproduced from ref. 59 with permission from Royal Society of Chemistry, copyright 2016.

framework (NMOF) of UiO-68 type by incorporating the chemotherapeutic agent DOX (doxorubicin) and a tumor-targeting agent, folic acid (FA).<sup>59</sup> The delivery system was administered *via* tail-vein injection. Through a comparison with free DOX and FA-unloaded  $DOX@Mi-UiO-68$ ,  $DOX@UiO-68-FA$  exhibited significantly higher antitumor efficacy. This conclusion was validated through various experiments, including cell imaging, standard 3-(4,5)-dimethylthiazol-2-yl-2,5-diphenyltetrazolium bromide (MTT) proliferation assays, and *in vivo* studies. The results from these experiments provided strong evidence of the improved therapeutic potential of the  $DOX@UiO-68-FA$  drug delivery system.

## 5.2. Delivery of miscellaneous drugs

The interactions between metal-organic frameworks (MOFs) and caffeine show great potential as carriers for the topical administration of caffeine.<sup>51</sup> Encapsulation of challenging cosmetic caffeine within porous MOFs achieves high payloads and fast kinetics. Release depends on the media: rapid release under serum-simulated conditions due to MOF degradation, and progressive release under topical conditions governed by caffeine mobility and MOF interactions. MIL-100 and UiO-66 hold promise for topical caffeine delivery with exceptional cosmetic payloads and controlled releases within 8–24 hours.

ZJU-101, a crystal with a size of approximately 300 nm, was utilized for loading diclofenac sodium, an anionic drug.<sup>52</sup> This positively charged host material exhibited a significant capacity for loading diclofenac sodium ( $\sim 0.546 \text{ g g}^{-1}$ ) through ion

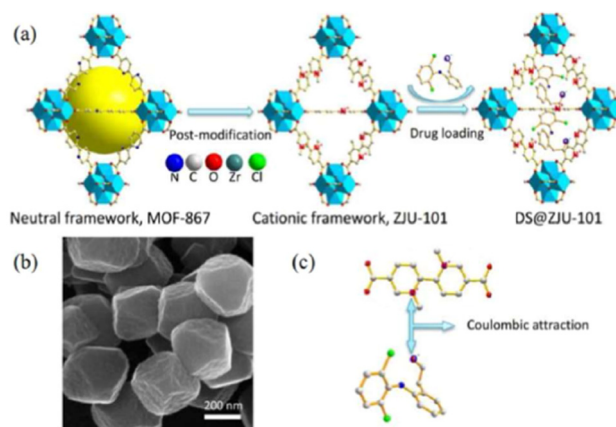


Fig. 12 (a) Schematic presentation of the post-modification and drug loading processes. (b) SEM images of ZJU-101. (c) The coulombic attraction between the ligand of the cationic framework and anionic drug. Reproduced from ref. 52 with permission from American Chemical Society, copyright 2016.

exchange and penetration procedures (Fig. 12). The release of the drug in inflamed tissues ( $pH = 5.4$ ) was more effective compared to normal tissues ( $pH = 7.4$ ), demonstrating a pH-responsive drug release based on physiological conditions. This selective drug release process was controlled by the exchange of anions between the anions in phosphate-buffered saline (PBS) and the coordinated/free diclofenac anions.

ZJU-800, a robust metal-organic framework (MOF) based on Zr clusters, has been discovered to possess exceptional drug loading capacity, reaching approximately 58.80 wt%.<sup>79</sup> By adjusting the compactness between the MOF and the drug diclofenac sodium (DS) through pressure, the release time of the drug can be controlled, ranging from 2 days to 8 days.

## 6. Zr-based MOFs as biomarkers

Coordination polymers, also known as metal-organic frameworks (MOFs), constitute a captivating class of hybrid materials, formed by connecting metal ions or metal clusters with molecular bridging ligands.<sup>80</sup> Notably, researchers have successfully demonstrated the capability to downsize these materials to the nanoscale, resulting in the creation of nanoscale coordination polymers (NCPs) that hold great promise for potential applications in biological and biomedical fields. In a noteworthy study, Wenbin Lin and colleagues<sup>81</sup> presented phosphorescent NCPs by employing the bridging ligand  $[Ru\{5,5'-(CO_2)-2-bpy\}(bpy)_2]$  (where bpy represents 2,2'-bipyridine) in conjunction with  $Zn^{2+}$  and  $Zr^{4+}$  as connecting points. The resulting NCPs exhibited intriguing phosphorescent properties, rendering them particularly intriguing for further exploration and their potential application in diverse areas. By incorporating specific metal ions and ligands, it becomes possible to design NCPs with tailored functionalities and characteristics, opening new avenues for advancements in nanomaterials and their potential use in biological and medical settings.

In the reported study, zinc (Zn) and zirconium (Zr) nano-scale coordination polymers (NCPs) were synthesized and characterized. The Zn NCP exhibited a dye loading of 78.7%, while the Zr NCP had a slightly lower dye loading of 57.4%. The Zr NCP was further stabilized by a silica coating and functionalized with poly(ethylene glycol) (PEG) and a targeting molecule, enabling its potential application in *in vitro* optical imaging of cancer cells. The Zn NCP, named NCP-1, was obtained with a yield of 54.3% through microwave heating of a solution containing L-H22 (a ligand), oxalic acid, and  $\text{Zn}(\text{NO}_3)_2$  in DMF (dimethylformamide) and water at 100 °C for 5 minutes. NCP-1 formed block-like particles with dimensions of approximately  $100 \times 100 \times 50$  nm upon isolation. On the other hand, the Zr NCP, named NCP-2, was produced by microwave heating of an acidic solution containing L-H22 and  $\text{ZrCl}_4$  in dmf at 100 °C for 10 minutes (Fig. 13). After centrifugation and washing with methanol and ethanol, dark orange particles of NCP-2 were obtained. However, it was observed that NCP-1 was not stable under the coating conditions, leading to the leaching of the L dye molecules from the particles and rendering the recovered particles nearly colorless. This instability was confirmed through SEM and energy-dispersive X-ray spectroscopy (EDS). To improve the stability of the NCPs, the researchers speculated that using  $\text{Zr}^{4+}$  ions instead of  $\text{Zn}^{2+}$  to connect the carboxylate groups of the L ligands could lead to the synthesis of more stable NCPs, similar to the UiO (University of Oslo) framework. Regarding the luminescent properties of NCP-2, it exhibited a luminescent quantum yield of 0.8% and an average luminescence lifetime of 107 ns at 630 nm. These properties suggest that NCP-2 could potentially be utilized in luminescence-based applications.

In 2010, Roming *et al.*<sup>83</sup> presented an intriguing system termed  $\text{ZrO}(\text{HPO}_4)_{1-x}(\text{FMN})_x$ , with  $x$  ranging from 0 to 1, composed of  $\text{ZrO}^{2+}$ ,  $\text{HPO}_4^{2-}$ , and  $\text{FMN}^{2-}$  (FMN, flavin mononucleotide, a derivative of vitamin B<sub>2</sub>). The notable characteristics of the system include very low solubility, which facilitates

nanoparticle formation and growth; the chemical inertness of zirconium phosphates, ensuring material stability and preventing undesired reactions; biocompatibility of all constituents, rendering them safe for diverse applications; and the ability to finely adjust the concentration of the fluorescent dye (FMN) from very low to molar levels, enabling customized optical properties. Particularly noteworthy is the innovative concept of combining an inorganic cation ( $\text{ZrO}^{2+}$ ) with an anionic fluorescent dye ( $\text{FMN}^{2-}$ ), a novel approach in luminescent materials at that time, holding promising potential for applications in nanomaterials and biocompatible luminescent materials. To achieve a rapid and streamlined synthesis process, forced hydrolysis in water was chosen as the preferred method. The main focus was on the formula denoted as  $\text{ZrO}(\text{HPO}_4)_{1-x}(\text{FMN})_x$  ( $x = 0-1$ ), aiming for a complete exchange of  $\text{HPO}_4^{2-}$  with  $\text{FMN}^{2-}$ . Remarkably, this successful exchange was observed for the first time in luminescent hybrid materials.<sup>83</sup> To accomplish this, two representative compounds were selected: zirconylflavin mononucleotide [ $\text{ZrO}(\text{FMN})$ ], which contains substantial amounts of the dye, and a “diluted” version  $\text{ZrO}(\text{HPO}_4)_{0.9}(\text{FMN})_{0.1}$ . Both compounds were easily obtained by mixing aqueous solutions of the starting materials, resulting in transparent yellow to orange suspensions that exhibited bright green emission under both ultraviolet (UV) light (at 366 nm) and blue light (at 380–450 nm) excitation. Due to the strong UV light absorption, only the part of the suspension close to the direction of incoming light displayed full luminescence. In the case of the blue light-emitting diode (LED), the scattering of blue light combined with the green emission led to partial additive color mixing, resulting in white light. The as-prepared suspensions typically contained solid contents of 1% by weight and demonstrated long-term stability over months. Despite the laboratory-scale synthesis (0.5–1.0 g amounts), straightforward scaling up is expected, as the material’s crystallinity and core-shell structures do not require special considerations. The size and shape of the as-prepared  $\text{ZrO}(\text{HPO}_4)_{1-x}(\text{FMN})_x$  was evaluated using dynamic light scattering (DLS), scanning electron microscopy (SEM), and transmission electron microscopy (TEM). DLS analysis revealed a relatively broad size distribution with a mean hydrodynamic diameter of 39–12 nm in water. However, redispersion in a more surface-active solvent, such as diethylene glycol (DEG), resulted in a much narrower size distribution (32–4 nm), indicating the presence of uniform primary particles with some agglomeration in water. Notably, all particles remained smaller than 100 nm even in water, and the synthesis process did not involve common colloidal stabilizers like long-chained amines or phosphines. Electron microscopy revealed that  $\text{ZrO}(\text{HPO}_4)_{1-x}(\text{FMN})_x$  had a spherical shape and a mean diameter of 25–40 nm. Finally, the specific surface area, measured using the Brunauer–Emmett–Teller (BET) method, confirmed the presence of a nanoscaled compound, with a value of  $115 \text{ m}^2 \text{ g}^{-1}$ .

$\text{ZrO}(\text{HPO}_4)_{1-x}(\text{FMN})_x$  nanoparticles have shown promise as effective tools for staining viable structures in whole organisms. To introduce specific targeting in organisms, organs, or cells, such as coupling specific antibodies, ligands, lectins, or receptor molecules, established techniques for functionalizing the

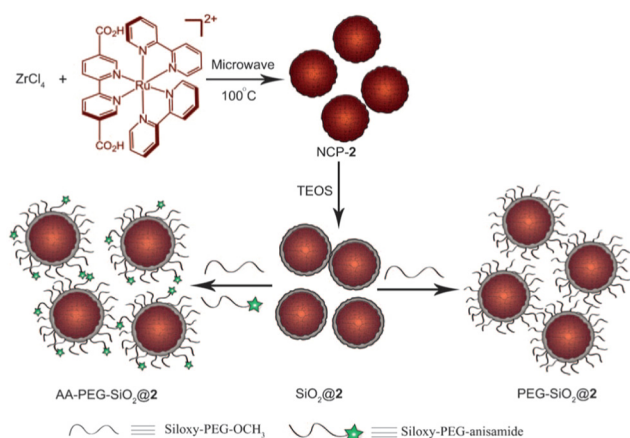


Fig. 13 Synthesis of NCP-2, coating of NCP-2 with a thin shell of silica, and further functionalization of  $\text{SiO}_2@2$  with PEG and PEG-anisamide. TEOS = tetraethylorthosilicate. Reproduced from ref. 82 with permission from WILEY-VCH Verlag GmbH & Co. KGaA, Weinheim, copyright 2011.

surface of semiconductor quantum dots and attaching specific linkers can now be applied to these nanoparticles. In addition to their green emission, the concept of dye-modified zirconium phosphates (DMZPs) has been expanded in a preliminary study to include other dye anions and different emission colors. For instance, introducing umbelliferone phosphate (UFP)<sup>2-</sup> resulted in obtaining noncrystalline nanoparticles with an approximate composition of “ZrO(UFP),” exhibiting blue emission under 366 nm excitation. Furthermore, it has been reported that ZrO(HPO<sub>4</sub>)<sub>1-x</sub>(FMN)<sub>x</sub> holds potential as a promising alternative to existing luminescent nanomaterials. Its use as a luminescent biomarker and its successful biocompatibility testing as a proof of concept in living mice and cells further support its potential applications. Additionally, DMZPs have been extended to display red and blue emission, as well as luminescence switching, adding to their versatility and potential for various biological and biomedical applications. Luminescent metal-organic frameworks (LMOFs) have garnered considerable interest as a distinctive group of sensing materials. In this particular study, the intrinsically fluorescent amino derivative of UiO-66 (UiO-66-NH<sub>2</sub>) was effectively utilized as a fluorescent probe for the sensitive and selective detection of phosphate anions in an aqueous medium.<sup>62</sup>

## 7. Multiple imaging (photodynamic therapy and biosensing)

Although nanoscale metal-organic frameworks (NMOFs) find extensive use in imaging techniques like computed tomography (CT), magnetic resonance imaging (MRI), and optical imaging, their application as *in vivo* tumor imaging agents remains relatively limited. For enhanced sensitivity and deeper signal penetration, positron emission tomography (PET) imaging is preferred due to its superior detection capabilities, even at picomolar concentrations, and its ability to provide quantitative data in both preclinical and clinical settings. Thus, there is a need for a biocompatible NMOF platform that can be employed in PET imaging and tumor targeting, facilitating future PET-guided cargo delivery to cancer sites. Among the available NMOFs, the zirconium-containing UiO-66 NMOF was selected as a template material due to its well-known optimal surface area and exceptional stability, facilitated by the presence of Zr<sub>6</sub>O<sub>4</sub>(OH)<sub>4</sub> connecting clusters. Surface engineering using pyrene-derived polyethylene glycol (PEG) was implemented to enhance UiO-66 stability and dispersity in biological media, while also providing additional functionalization sites for the integration of tumor-targeting molecules.<sup>63</sup> Chen *et al.* presented a study on the production and characterization of an intrinsically radioactive nanoscale metal-organic framework (nMOF) named <sup>89</sup>Zr-UiO-66.<sup>84</sup> The nMOF was incorporated with the positron-emitting isotope zirconium-89 (<sup>89</sup>Zr) to enable PET imaging. Further functionalization of <sup>89</sup>Zr-UiO-66 was carried out using pyrene-derived polyethylene glycol (Py-PGA-PEG) and conjugation with a peptide ligand (F3) targeted to nucleolin, specifically for triple-negative breast tumors. Additionally, the nMOF was loaded with doxorubicin (DOX) as both a therapeutic

and a fluorescence visualizer. The functionalized <sup>89</sup>Zr-UiO-66 demonstrated robust radiochemical and material stability in various biological media. Based on cellular targeting and *in vivo* PET imaging results, it was concluded that the <sup>89</sup>Zr-UiO-66/Py-PGA-PEG-(F3) complex serves as a promising image-guidable, tumor-selective cargo delivery nanoplatform. This study presents a potential avenue for the development of targeted cancer therapies using nMOFs as imaging agents and drug carriers simultaneously.

Biological thiols, such as cysteine (Cys) and glutathione (GSH), play crucial roles in numerous biological processes within living organisms. Cys acts as a precursor to the antioxidant GSH, and their levels can undergo significant changes in response to oxidative stress associated with toxic insults, bacterial infections, and various diseases. Deficiencies in Cys can lead to various aberrations, including decreases in hematopoiesis, loss of leukocytes, and psoriasis, among others. On the other hand, GSH is involved in several important functions in the body, including the regulation of the redox environment in cells. In this context, Mi-UiO-66 and Mi-UiO-67<sup>64</sup> were developed as fluorescent probes for detecting Cys and GSH. These probes exhibited high sensitivity (10–11 M) and selectivity for Cys and GSH, making them effective tools for detecting these thiols. Moreover, the fluorescence imaging of Cys and GSH in living cells was convincingly demonstrated, showcasing their potential for *in vivo* applications in studying thiol-related biological processes.

The development of a photosensitizing system that can efficiently control the generation of singlet oxygen (<sup>1</sup>O<sub>2</sub>) is of significant interest in the field of photodynamic therapy (PDT). Recently, several photosensitizer-photochromic-switch dyads have been proposed as a potential means of achieving controlled <sup>1</sup>O<sub>2</sub> generation in PDT. Among these, a Zr-MOF (Metal-Organic Framework) nanoplatform has been investigated, demonstrating energy transfer-based <sup>1</sup>O<sub>2</sub> controlled PDT. Zhou *et al.* showed the energy-transfer-based <sup>1</sup>O<sub>2</sub>-controlled PDT using a Zr-MOF as a nanocarrier.<sup>85</sup> The photosensitizing system, installed in the MOF pores, allows the control of <sup>1</sup>O<sub>2</sub> generation using a photochromic switch. In this study, a widely employed photosensitizer, porphyrin, and a DTE (diarylethene) derivative were successfully incorporated into the Zr-MOF, with adjustable ratios. This strategy enables the fine-tuning of energy transfer for <sup>1</sup>O<sub>2</sub> control by adjusting the ratios between the two dyes incorporated into the MOF. Furthermore, the dyad was effectively delivered into cells, demonstrating successful cellular uptake and potential for targeted PDT applications.<sup>86</sup> This represents a promising approach for achieving controlled <sup>1</sup>O<sub>2</sub> generation in PDT using Zr-MOF nanocarriers. Adsorption behavior of the uremic toxins, *p*-cresyl sulfate, indoxyl sulfate, and hippuric acid, from human serum albumin in zirconium-pyrene-based metal-organic frameworks (MOFs) NU-1000 (Fig. 14), offers the highest toxin removal efficiently.<sup>63</sup>

The recent application of metal-organic frameworks (MOFs) as biomimetic mineralization to living cells and viruses opens up numerous exciting possibilities in cell biology and biotechnology (Fig. 15). The encapsulation processes introduced

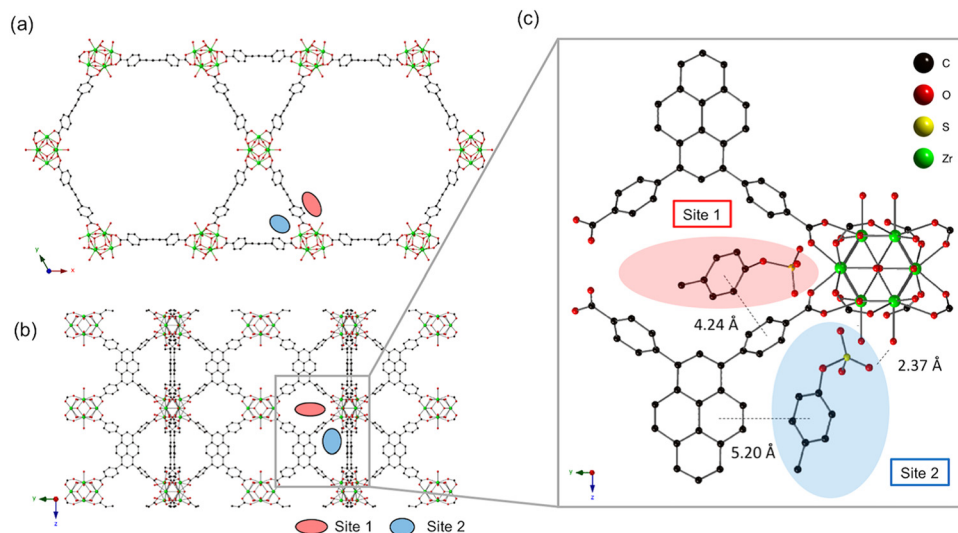


**Fig. 14** (a) The crystal structure of NU-1000 viewed down the *c*-axis and (b) an orthogonal view prior to *p*-cresyl sulfate exposure (each adsorption site is depicted by a colored oval). (c) Optimized geometry of *p*-cresyl sulfate-pyrene and  $Zr_6$  node domains after *p*-cresyl sulfate adsorption. For clarity, only one orientation of *p*-cresyl sulfate is extracted at each site, and potassium counterions and hydrogens are omitted. Reproduced from ref. 63 with permission from American Chemical Society, copyright 2019.

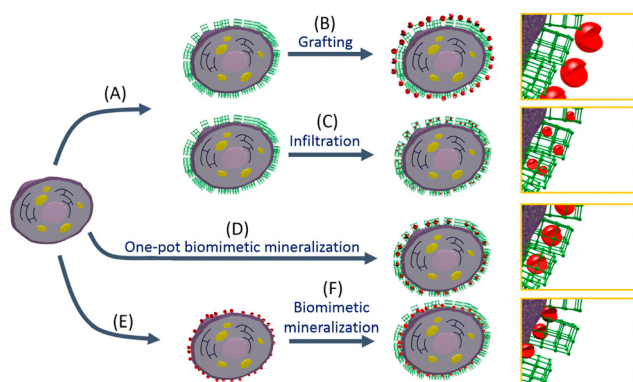


**Fig. 15** (A) Cell can be coated with a metal–organic framework (MOF) via biomimetic mineralization, and then (B) enzymes can be grafted to the surface of the framework. (C) If the framework pore and pore aperture size are large enough, enzymes can be introduced into the MOF via infiltration. (D) Biomimetic mineralization procedure in the presence of enzyme results in a shell where the biomacromolecules are encapsulated in a single step. Finally, (E) enzymes can be directly immobilized on the surface of the cell, followed by (F) biomimetic mineralization to afford a cell/enzyme system. Reproduced from ref. 87 with permission from American Chemical Society, copyright 2018.

through this approach provide a protective shield to cells and viruses, safeguarding them from inhospitable external environments that could lead to cell death or virus deprivation. However, it is worth noting that the research field is still in its early stages, and further investigations involving different types of cells, viruses, and MOFs are needed to fully demonstrate the versatility and potential of this technique.<sup>87</sup>

Luminescent metal–organic frameworks (LMOFs) have emerged as valuable materials for selectively recognizing various molecules and ions through detectable luminescence responses. While MOFs have been successfully utilized as NO

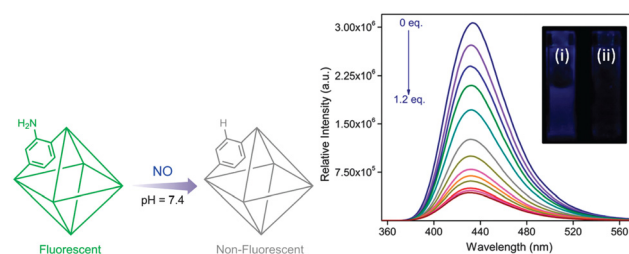


**Fig. 16** Schematic illustration of nitric oxide detection by a functionalized MOF. Change in fluorescence intensity of 1-NH<sub>2</sub> upon incremental addition of 0.1 mM NO solution. Inset – fluorescence of 1-NH<sub>2</sub> (i) before and (ii) after NO addition. Reproduced from ref. 88 with permission from American Chemical Society, copyright 2019.

storage and delivery agents, the extension of common approaches for NO detection to MOF-based sensors has been relatively scarce. A notable example is UiO-66@NH<sub>2</sub> (1-NH<sub>2</sub>), where the desolvated phase of the MOF dispersed in HEPES buffer (10 mM, pH 7.4) was excited at 325 nm, and the emission profile was recorded between 340 and 630 nm before and after NO addition (Fig. 16). An intriguing observation was made, showing a smooth emission curve peaking at 432 nm, which underwent a significant change upon treatment with NO.<sup>88</sup> This discovery stimulates further research in the field of Zr-based MOF sensors for NO detection, pushing towards the goal of developing probes for relevant biological applications.

## 8. Zr-based MOFs for health fortification

Zirconium-based metal–organic frameworks (Zr-MOFs) have emerged as a bioinspired class of materials with remarkable



Table 5 Zr-MOF as catalyst for the hydrolysis of nerve agents and nerve agent stimulants

MOF	Linker	Base	Simulant [ $t_{1/2}$ (min)]	Nerve agent [ $t_{1/2}$ (min)]	Ref.
UiO-66	BDC		DMNP [ $\sim 10$ d]	GD [ $< 0.5$ d]; VX [ $< 0.5$ d]	88
UiO-66-NH <sub>2</sub>	BDC-2-NH <sub>2</sub>		DMNP [ $\sim 3$ d]	GD [ $< 0.5$ d]; VX [ $\sim 1$ d]	88
NU-1000	H <sub>4</sub> TBAPy		DMNP [ $> 30$ d]	GD [ $\sim 2$ d]; VX [ $\sim 3$ d]	88
MOF-808	BTC <sup>3-</sup>	[BA-morph]	DMNP [9]	VX [ $< 1$ ]	89
NU-901	H <sub>4</sub> TBAPy	[BA-morph]	DMNP [1080]		89
NU-901	H <sub>4</sub> TBAPy	PAMAM	DMNP [1.1]		90
NU-901	H <sub>4</sub> TBAPy	B-PEI	DMNP [1.9]		90
NU-1000-dehyd	H <sub>4</sub> TBAPy	L-PEI	DMNP [1.8]	GD [4.8]	91
NU-1000-dehyd	H <sub>4</sub> TBAPy	L-PEI	VX [12.7]		91
UiO-66	BDC	L-PEI	DMNP [2.7]		92
UiO-66	BDC	B-PEI	DMNP [ $> 60$ ]		92
NU-1600	H <sub>6</sub> PET-1 R = -COOH	L-PEI	DMNP [3]	GD [12]	37
NU-1601	H <sub>6</sub> PET-2 R = -C <sub>6</sub> H <sub>4</sub> -4- COOH		DMNP [3.2]		37
NU-1602	H <sub>6</sub> PET-3 R = -CC-C <sub>6</sub> H <sub>4</sub> -4- COOH		DMNP [2.2]		37
NU-1002- <i>m</i> -NH <sub>2</sub>	H <sub>4</sub> TBAPy- <i>m</i> -NH <sub>2</sub>		DMNP [2.8]		93
NU-1002- <i>o</i> -NH <sub>2</sub>	H <sub>4</sub> TBAPy- <i>o</i> -NH <sub>2</sub>		DMNP [1.2]		93
Spiro-MOF	Spirof-L		DMNP [7.5]		94
PCN-777	TATB		DENP [3.6]	GA [ $< 1$ ], GD [ $< 1$ ]	95
NU-1400	TPTC		DMNP [3]		96

catalytic properties for the hydrolysis of nerve agents. Nerve agents directly interfere with the central nervous system by binding to the active site of acetylcholinesterase, an enzyme responsible for regulating choline ester-based neurotransmitters crucial for voluntary muscle control. This binding inhibits the enzyme's proper function, leading to the accumulation of acetylcholine neurotransmitter, causing continuous muscle contractions, paralysis, and ultimately, death. Organophosphorus nerve agents like Tabun (GA), Sarin (GB), Soman (GD), and *O*-ethyl *S*-diisopropylaminomethylmethylphosphonothiolate (VX), along with nerve agent stimulants such as dimethyl methyl phosphonates (DMMP), diisopropylfluorophosphate (DIFP), dimethyl-4-nitrophenyl phosphonates (DMNP), and diethyl-4-nitrophenyl phosphonates (DENP), are some of the most toxic chemicals known to humanity. Despite international bans, their unfortunate recent use has underscored the urgent need to develop effective materials for degrading these nerve agents.

Zr-MOFs have proven to be highly effective in rapidly hydrolyzing these nerve agents, significantly reducing their toxicity. The effectiveness of Zr-MOFs in rapidly reducing the toxicity of nerve agents is substantiated by empirical evidence, as indicated in Table 5. Their bioinspired nature and exceptional catalytic performance make them promising candidates for addressing the critical challenge of neutralizing and detoxifying these deadly compounds. In the fight against chemical warfare agents, the development of such advanced materials represents a crucial step towards enhancing global security and safeguarding human health.

## 9. Conclusions

Zirconium-based metal-organic frameworks (Zr-MOFs) or coordination polymers offer a range of advantages for the

adsorption and controlled release of biomolecules, setting them apart from other drug carriers like inorganic porous solids or organic polymers. The tunable composition, structure, pore size, and volume of Zr-MOFs, along with easy functionalization, flexible networks, and accessible metal sites, make them highly suitable for such applications. Moreover, their biodegradable nature can be tailored by carefully selecting the metal, linker, and structure, enabling degradation in body fluids over varying timeframes, from minutes to weeks.

An innovative approach to drug release involves designing bioactive MOFs based on the drug itself as the linker, allowing its release through the degradation of the Zr-MOF. Alternatively, a bioactive/non-toxic metal like Zr can be used as the inorganic cation, adding antibacterial activity or imaging properties. At the nanometric scale, various synthesis techniques such as microwave-assisted hydro or solvothermal methods, sonothermal methods, and reverse emulsion techniques enable diverse administration routes (intravenous, ocular, *etc.*) and facilitate various formulations like pellets, thin films, gels, composites, and more. Although the surface modification of Zr-MOF nanoparticles is still in its early stages, it holds great promise as it can modulate MOFs' biodistribution by influencing bioadhesion, stealth, targeting, and stability.

Zr-MOFs have demonstrated remarkable loading capacities for therapeutic molecules, including drugs, cosmetics, and biological gases, with the added benefit of controllable release of their cargo. These porous Zr-MOFs have successfully entrapped challenging drug and biogas molecules, allowing for their controlled and gradual release in *in vitro* experiments. Such advancements pave the way for promising applications in drug delivery and biomedicine, offering potential breakthroughs in controlled and efficient therapeutic treatments.

## Abbreviations

BDC <sup>2-</sup>	Terephthalate
BPDC <sup>2-</sup>	Biphenyl-4,4'-dicarboxylate
TPDC <sup>2-</sup>	[1,1':4',4''-Terphenyl]-4,4''-dicarboxylate
TBAPy <sup>4-</sup>	1,3,6,8-Tetrakis( <i>p</i> -benzoate)pyrene
Py-XP <sup>4-</sup>	4,4',4'',4'''-(Pyrene-1,3,6,8-tetra-yl) tetrakis(2',5'-dimethyl-[1,10-biphenyl]-4-carboxylate)
Por-PP <sup>4-</sup>	<i>Meso</i> -tetrakis-(4-carboxylatebiphenyl)-porphyrin
PTBA <sup>4-</sup>	4-[2-[3,6,8-Tris[2-(4-carboxylatephenyl)-ethynyl]-pyren-1-yl]ethynyl]-benzoate
Py-PTP <sup>4-</sup>	4,4',4'',4'''-(Pyrene-1,3,6,8-tetra-yl)tetrakis(benzene-4,1-diyl)tetrakis(ethyne-1-diyl)tetrabenzoate
Por-PTP <sup>4-</sup>	<i>Meso</i> -tetrakis-(4-((phenyl)ethynyl)benzoate)porphyrin
FUM <sup>2-</sup>	fumarate
PZDC <sup>2-</sup>	1H-pyrazole-3,5-dicarboxylate
BTC <sup>3-</sup>	Benzene-1,3,5-tricarboxylate
MTB <sup>4-</sup>	4,4',4'',4'''-Methanetetrayltetrabenzoate
TCPP <sup>4-</sup>	<i>Meso</i> -tetrakis(4-carboxylatephenyl)porphyrin
XF <sup>4-</sup>	4,40-((1E,10E)-(2,5-bis((4-carboxylatephenyl)ethynyl)-1,4-phenylene)bis(ethene-2,1-diyl))dibenzoate
BPYDC <sup>2-</sup>	2,20-Bipyridine-5,50-dicarboxylate
ABDC <sup>2-</sup>	4,4-Azobenzenedicarboxylate
TCBPP <sup>4-</sup>	Tetrakis(4-carboxylatebiphenyl)porphyrin
ETTC <sup>4-</sup>	4,4',4'',4'''-(Ethene-1,1,2,2-tetra-yl)tetrabiphenyl-4-carboxylate
TDC <sup>2-</sup>	2,5-Thiophenedicarboxylate
MTBC <sup>4-</sup>	4,4',4'',4'''-Methanetetrayltetrabiphenyl-4-carboxylate
TATB <sup>3-</sup>	4',4'',4'''-s-triazine-2,4,6-triyl-tribenzoate
DTTDC <sup>2-</sup>	Dithieno[3,2- <i>b</i> ;20,30- <i>d</i> ]-thiophene-2,6-dicarboxylate
2,6-NDC <sup>2-</sup>	Naphthalene-2,6-dicarboxylate
FDCA <sup>2-</sup>	9-Fluorenone-2,7-dicarboxylate
DTDAO <sup>2-</sup>	Dibenzo[ <i>b,d</i> ]thiophene-3,7-dicarboxylate
EDDB <sup>2-</sup>	5,5-dioxide
H <sub>3</sub> pgal	4',4''-(Ethyne-1,2-diyl)dibenzoate
H <sub>4</sub> gal	Pyrogallol
H <sub>2</sub> sal	Gallic acid
H <sub>6</sub> TzGal	Salicylic acid
BTB <sup>3-</sup>	5,5'-(1,2,4,5-Tetrazine-3,6-diyl)bis(benzene-1,2,3-triyl)
TTMC <sup>2-</sup>	5'-[4-Carboxyphenyl][1,10:300,100-terphenyl]-4,400-dicarboxylate
ABDC <sup>2-</sup>	(2E,4E)-hexa-2,4-dienedioate
H <sub>6</sub> BTBP	Azobenzenedicarboxylate
H <sub>6</sub> TTBMP	1,3,5-Tris(4-phosphonophenyl)benzene
PEDC <sup>2-</sup>	2,4,6-Tris(4-(phosphonomethyl)phenyl)-1,3,5-triazine
BPV <sup>2-</sup>	4,4'-(1,4-Phenylenebis-(ethyne-2,1-diyl))dibenzoate
BPHV <sup>2-</sup>	5,5'-Bis(carboxylateethenyl)-2,20-bipyridine
	4,4'-Bis(carboxylateethenyl)-1,10-biphenyl

TPHN <sup>2-</sup>	4,40-Bis(carboxylatephenyl)-2-nitro-1,10-biphenyl
ADC <sup>2-</sup>	9,10-Anthracenyl bis(benzoate)
DTDC <sup>2-</sup>	3,4-Dimethylthieno[2,3- <i>b</i> ]thiophene-2,5-dicarboxylate
TCPS <sup>4-</sup>	Tetrakis(4-carboxyphenyl) silane
BTBA <sup>4-</sup>	4',4'',4''',4''''-(Biphenyl-3,3',5,5'-tetrayltetrakis(ethyne-2,1-diyl))tetrabenzoate
AP <sup>2-</sup>	1,6-Adipate

## Conflicts of interest

There are no conflicts of interest to declare.

## References

- 1 R. Di Maggio, R. Camprostrini and G. Guella, *Chem. Mater.*, 1998, **10**, 3839–3847.
- 2 M. Roming, H. Lünsdorf, K. E. J. Dittmar and C. Feldmann, *Angew. Chem., Int. Ed.*, 2010, **49**, 632–637.
- 3 M. Kim, S. J. Garibay and S. M. Cohen, *Inorg. Chem.*, 2011, **50**, 729–731.
- 4 D. Liu, R. C. Huxford and W. Lin, *Angew. Chem., Int. Ed.*, 2011, **50**, 3696–3700.
- 5 A. Schaate, P. Roy, T. Preufse, S. J. Lohmeier, A. Godt and P. Behrens, *Chem. – Eur. J.*, 2011, **17**, 9320–9325.
- 6 H.-M. Meng, T. Fu, X.-B. Zhang, N.-N. Wang, W. Tan, G.-L. Shen and R.-Q. Yu, *Anal. Chem.*, 2012, **84**, 2124–2128.
- 7 G. Wißmann, A. Schaate, S. Lilienthal, I. Bremer, A. M. Schneider and P. Behrens, *Microporous Mesoporous Mater.*, 2012, **152**, 64–70.
- 8 V. Bon, V. Senkovskyy, I. Senkovska and S. Kaskel, *Chem. Commun.*, 2012, **48**, 8407–8409.
- 9 W. Liang, R. Babarao and D. M. D'Alessandro, *Inorg. Chem.*, 2013, **52**, 12878–12880.
- 10 D. Feng, W. C. Chung, Z. Wei, Z. Y. Gu, H. L. Jiang, Y. P. Chen, D. J. Darensbourg and H. C. Zhou, *J. Am. Chem. Soc.*, 2013, **135**, 17105–17110.
- 11 W. Chen, Y. Cheng and B. Wang, *Angew. Chem., Int. Ed.*, 2012, **51**, 5293–5295.
- 12 R. Vismara, C. Di Nicola, R. G.-S. Millán, K. V. Domasevich, C. Pettinari, J. A. R. Navarro and S. Galli, *Nano Res.*, 2021, **14**, 532–540.
- 13 G. Ayoub, T. Islamoglu, S. Goswami, T. Frišćić and O. K. Farha, *ACS Appl. Mater. Interfaces*, 2019, **11**, 15788–15794.
- 14 T. Duerinck, R. Bueno-Perez, F. Vermoortele, D. E. De Vos, S. Calero, G. V. Baron and J. F. M. Denayer, *J. Phys. Chem. C*, 2013, **117**, 12567–12578.
- 15 K. Matsuyama, N. Hayashi, M. Yokomizo, T. Kato, K. Ohara and T. Okuyama, *J. Mater. Chem. B*, 2014, **2**, 7551–7558.
- 16 J. Ren, T. Segakweng, H. W. Langmi, N. M. Musyoka, B. C. North, M. Mathe and D. Bessarabov, *Int. J. Mater. Res.*, 2014, **105**, 516–519.
- 17 P. T. Phan, J. Hong, N. Tran and T. H. Le, *Nanomaterials*, 2023, **13**, 352.

- 18 O. Karagiari, W. Bury, J. E. Mondloch, J. T. Hupp and O. K. Farha, *Angew. Chem., Int. Ed.*, 2014, **53**, 4530–4540.
- 19 H. Reinsch, B. Bueken, F. Vermoortele, I. Stassen, A. Lieb, K.-P. Lillerud and D. De Vos, *CrystEngComm*, 2015, **17**, 4070–4074.
- 20 I. Erucar and S. Keskin, *Ind. Eng. Chem. Res.*, 2016, **55**, 1929–1939.
- 21 C. Koschnick, M. W. Terban, R. Frison, M. Etter, F. A. Böhm, D. M. Proserpio, S. Krause, R. E. Dinnebier, S. Canossa and B. V. Lotsch, *J. Am. Chem. Soc.*, 2023, **145**, 10051–10060.
- 22 F. Trouselet, A. Archereau, A. Boutin and F.-X. Coudert, *J. Phys. Chem. C*, 2016, **120**, 24885–24894.
- 23 M. Viciano-Chumillas, X. Liu, A. Leyva-Pérez, D. Armentano, J. Ferrando-Soria and E. Pardo, *Coord. Chem. Rev.*, 2022, **451**, 214273.
- 24 J. H. Cavka, S. Jakobsen, U. Olsbye, N. Guillou, C. Lamberti, S. Bordiga and K. P. Lillerud, *J. Am. Chem. Soc.*, 2008, **130**, 13850–13851.
- 25 J. Ren, T. Segakweng, H. W. Langmi, N. M. Musyoka, B. C. North, M. Mathe and D. Bessarabov, *Int. J. Mater. Res.*, 2014, **105**, 516–519.
- 26 Q. Yang, S. Vaesen, F. Ragone, A. D. Wiersum, D. Wu, A. Lago, T. Devic, C. Martineau, F. Taulelle, P. L. Llewellyn, H. Jovic, C. Zhong, C. Serre, G. De Weireld and G. Maurin, *Angew. Chem., Int. Ed.*, 2013, **52**, 10316–10320.
- 27 Y. Bai, Y. Dou, L.-H. Xie, W. Rutledge, J.-R. Li and H.-C. Zhou, *Chem. Soc. Rev.*, 2016, **45**, 2327–2367.
- 28 S. Pullen, H. Fei, A. Orthaber, S. M. Cohen and S. Ott, *J. Am. Chem. Soc.*, 2013, **135**, 16997–17003.
- 29 H. Fei and S. M. Cohen, *J. Am. Chem. Soc.*, 2015, **137**, 2191–2194.
- 30 X. Zhu, J. Gu, Y. Wang, B. Li, Y. Li, W. Zhao and J. Shi, *Chem. Commun.*, 2014, **50**, 8779–8782.
- 31 Y.-A. Li, C.-W. Zhao, N.-X. Zhu, Q.-K. Liu, G.-J. Chen, J.-B. Liu, X.-D. Zhao, J.-P. Ma, S. Zhang and Y.-B. Dong, *Chem. Commun.*, 2015, **51**, 17672–17675.
- 32 S. Nagata, K. Kokado and K. Sada, *Chem. Commun.*, 2015, **51**, 8614–8617.
- 33 W. Morris, W. E. Briley, E. Auyeung, M. D. Cabezas and C. A. Mirkin, *J. Am. Chem. Soc.*, 2014, **136**, 7261–7264.
- 34 C. He, K. Lu, D. Liu and W. Lin, *J. Am. Chem. Soc.*, 2014, **136**, 5181–5184.
- 35 S.-Y. Li, H. Cheng, B.-R. Xie, W.-X. Qiu, J.-Y. Zeng, C.-X. Li, S.-S. Wan, L. Zhang, W.-L. Liu and X.-Z. Zhang, *ACS Nano*, 2017, **11**, 7006–7018.
- 36 D. Feng, H.-L. Jiang, Y.-P. Chen, Z.-Y. Gu, Z. Wei and H.-C. Zhou, *Inorg. Chem.*, 2013, **52**, 12661–12667.
- 37 Z. Chen, P. Li, X. Wang, K. I. Otake, X. Zhang, L. Robison, A. Atilgan, T. Islamoglu, M. G. Hall, G. W. Peterson, J. F. Stoddart and O. K. Farha, *J. Am. Chem. Soc.*, 2019, **141**, 12229–12235.
- 38 K. O. Kirlikovali, Z. Chen, T. Islamoglu, J. T. Hupp and O. K. Farha, *ACS Appl. Mater. Interfaces*, 2020, **12**, 14702–14720.
- 39 D. A. Gomez-Gualdrón, O. V. Gutov, V. Krungleviciute, B. Borah, J. E. Mondloch, J. T. Hupp, T. Yildirim, O. K. Farha and R. Q. Snurr, *Chem. Mater.*, 2014, **26**, 5632–5639.
- 40 C. Weyh, K. Krüger, P. Peeling and L. Castell, The Role of Minerals in the Optimal Functioning of the Immune System, *Nutrients*, 2022, **14**(3), 644, DOI: [10.3390/nu14030644](https://doi.org/10.3390/nu14030644).
- 41 K. Jomova, M. Makova, S. Y. Alomar and S. H. Alwasel, *Chem.-Biol. Interact.*, 2022, **367**, 110173.
- 42 M. Jaishankar, T. Tseten, N. Anbalagan, B. B. Mathew and K. N. Beeregowda, *Interdiscip. Toxicol.*, 2014, **7**(2), 60–72.
- 43 M. Balali-Mood, K. Naseri, Z. Tahergorabi, M. R. Khazdair and M. Sadeghi, *Front. Pharmacol.*, 2021, **12**, 643972, DOI: [10.3389/fphar.2021.643972](https://doi.org/10.3389/fphar.2021.643972).
- 44 I. Abánades Lázaro and R. S. Forgan, *Coord. Chem. Rev.*, 2019, **380**, 230–259.
- 45 S. Ghosh, A. Sharma and G. Talukder, Zirconium. An abnormal trace element in biology, *Biol. Trace Elem. Res.*, 1992, **35**(3), 247, DOI: [10.1007/BF02783770](https://doi.org/10.1007/BF02783770).
- 46 T. Sun, X. Liu, X. Zhan, L. Ou and R. Lai, *Process Saf. Environ. Prot.*, 2021, **147**, 134–145.
- 47 P. Horcajada, R. Gref, T. Baati, P. K. Allan, G. Maurin, P. Couvreur, G. Férey, R. E. Morris and C. Serre, *Chem. Rev.*, 2012, **112**, 1232–1268.
- 48 Z. Sun, T. Li, T. Mei, Y. Liu, K. Wu, W. Le and Y. Hu, *J. Mater. Chem. B*, 2023, **11**, 3273–3294.
- 49 C. P. Raptopoulou, Metal-Organic Frameworks: Synthetic Methods and Potential Applications, *Materials*, 2021, **14**(2), 310.
- 50 Harrison D. Lawson, S. Patrick Walton and Christina Chan, Metal-Organic Frameworks for Drug Delivery: A Design Perspective, *ACS Appl. Mater. Interfaces*, 2021, **13**(6), 7004–7020.
- 51 D. Cunha, M. Ben Yahia, S. Hall, S. R. Miller, H. Chevreau, E. Elkaïm, G. Maurin, P. Horcajada and C. Serre, *Chem. Mater.*, 2013, **25**, 2767–2776.
- 52 Y. Yang, Q. Hu, Q. Zhang, K. Jiang, W. Lin, Y. Yang, Y. Cui and G. Qian, *Mol. Pharmaceutics*, 2016, **13**, 2782–2786.
- 53 S. Tai, W. Zhang, J. Zhang, G. Luo, Y. Jia, M. Deng and Y. Ling, *Microporous Mesoporous Mater.*, 2016, **220**, 148–154.
- 54 L. L. Tan, H. Li, Y. Zhou, Y. Zhang, X. Feng, B. Wang and Y. W. Yang, *Small*, 2015, **11**, 3807–3813.
- 55 C. Orellana-Tavra, E. F. Baxter, T. Tian, T. D. Bennett, N. K. H. Slater, A. K. Cheetham and D. Fairen-Jimenez, *Chem. Commun.*, 2015, **51**, 13878–13881.
- 56 X. Meng, B. Gui, D. Yuan, M. Zeller and C. Wang, *Sci. Adv.*, 2016, **2**, e1600480.
- 57 H.-X. Zhao, Q. Zou, S.-K. Sun, C. Yu, X. Zhang, R.-J. Li and Y.-Y. Fu, *Chem. Sci.*, 2016, **7**, 5294–5301.
- 58 W. Wang, L. Wang, Z. Li and Z. Xie, *Chem. Commun.*, 2016, **52**, 5402–5405.
- 59 Y.-A. Li, X.-D. Zhao, H.-P. Yin, G.-J. Chen, S. Yang and Y.-B. Dong, *Chem. Commun.*, 2016, **52**, 14113–14116.
- 60 M. H. Teplensky, M. Fantham, P. Li, T. C. Wang, J. P. Mehta, L. J. Young, P. Z. Moghadam, J. T. Hupp, O. K. Farha, C. F. Kaminski and D. Fairen-Jimenez, *J. Am. Chem. Soc.*, 2017, **139**, 7522–7532.
- 61 C. Orellana-Tavra, S. Haddad, R. J. Marshall, I. Abánades Lázaro, G. Boix, I. Imaz, D. MasPOCH, R. S. Forgan and D. Fairen-Jimenez, *ACS Appl. Mater. Interfaces*, 2017, **9**, 35516–35525.

- 62 J. Yang, Y. Dai, X. Zhu, Z. Wang, Y. Li, Q. Zhuang, J. Shi and J. Gu, *J. Mater. Chem. A*, 2015, **3**, 7445–7452.
- 63 S. Kato, K. I. Otake, H. Chen, I. Akpınar, C. T. Buru, T. Islamoglu, R. Q. Snurr and O. K. Farha, *J. Am. Chem. Soc.*, 2019, **141**, 2568–2576.
- 64 H. L. Jiang, D. Feng, K. Wang, Z. Y. Gu, Z. Wei, Y. P. Chen and H. C. Zhou, *J. Am. Chem. Soc.*, 2013, **135**, 13934–13938.
- 65 Z. Wei, Z.-Y. Gu, R. K. Arvapally, Y.-P. Chen, R. N. McDougald, Jr., J. F. Ivy, A. A. Yakovenko, D. Feng, M. A. Omary and H.-C. Zhou, *J. Am. Chem. Soc.*, 2014, **136**, 8269–8276.
- 66 D. B. Trushina, A. Y. Sapach, O. A. Burachevskaia, P. V. Medvedev, D. N. Khmelenin, T. N. Borodina, M. A. Soldatov and V. V. Butova, *Pharmaceutics*, 2022, **14**.
- 67 M. Parsaei and K. Akhbari, *ACS Omega*, 2023, **8**, 41321–41338.
- 68 K. Chattopadhyay, M. Mandal and D. Kumar Maiti, *Mater. Adv.*, 2024, **5**, 51–67.
- 69 K. A. Mocniak, I. Kubajewska, D. E. M. Spillane, G. R. Williams and R. E. Morris, *RSC Adv.*, 2015, **5**, 83648–83656.
- 70 X. Meng Bo Gui, D. Yuan, M. Zeller and C. Wang, *Sci. Adv.*, 2016, **2**, e1600480, DOI: [10.1126/sciadv.1600480](https://doi.org/10.1126/sciadv.1600480).
- 71 C. He, K. Lu and W. Lin, *J. Am. Chem. Soc.*, 2014, **136**, 12253–12256.
- 72 R. C. Huxford, K. E. DeKrafft, W. S. Boyle, D. Liu and W. Lin, *Chem. Sci.*, 2012, **3**, 198–204.
- 73 S. Nagata, K. Kokado and K. Sada, *CrystEngComm*, 2020, **22**, 1106–1111.
- 74 M. Filippousi, S. Turner, K. Leus, P. I. Sifaka, E. D. Tseligka, M. Vandichel, S. G. Nanaki, I. S. Vizirianakis, D. N. Bikiaris, P. Van Der Voort and G. Van Tendeloo, *Int. J. Pharm.*, 2016, **509**(1–2), 208–218.
- 75 H.-X. Zhao, Q. Zou, S.-K. Sun, C. Yu, X. Zhang, R.-J. Lia and Y.-Y. Fu, *Chem. Sci.*, 2016, **7**, 5294–5301.
- 76 L.-L. Tan, N. Song, S. X.-A. Zhang, H. Li, B. Wang and Y.-W. Yang, *J. Mater. Chem. B*, 2016, **4**, 135–140.
- 77 G. Gupta, Y. Sun, A. Das, P. J. Stang and C. Y. Lee, BODIPY based Metal-Organic Macrocycles and Frameworks: Recent Therapeutic Developments, *Coord. Chem. Rev.*, 2022, **452**, 214308, DOI: [10.1016/j.ccr.2021.214308](https://doi.org/10.1016/j.ccr.2021.214308).
- 78 X. Chen, B. B. Mendes, Y. Zhuang, J. Coniot, S. Mercado Argandona, F. Melle, D. P. Sousa, D. Perl, A. Chivu, H. K. Patra, W. Shepard, J. Conde and D. Fairen-Jimenez, *J. Am. Chem. Soc.*, 2024, **146**(2), 1644–1656, DOI: [10.1021/jacs.3c12416](https://doi.org/10.1021/jacs.3c12416).
- 79 K. Jiang, L. Zhang, Q. Hu, D. Zhao, T. Xia, W. Lin, Y. Yang, Y. Cui, Y. Yang and G. Qian, *J. Mater. Chem. B*, 2016, **4**, 6398–6401.
- 80 S. R. Batten, B. Chen and J. J. Vittal, *ChemPlusChem*, 2016, **81**(8), 669–670.
- 81 D. Micheroni, Z. Lin, Y. S. Chen and W. Lin, *Inorg. Chem.*, 2019, **58**, 7645–7648.
- 82 D. Liu, R. C. Huxford and W. Lin, *Angew. Chem., Int. Ed.*, 2011, **50**, 3696–3700.
- 83 M. Roming, H. Lünsdorf, K. E. Dittmar and C. Feldmann, *Angew. Chem., Int. Ed.*, 2010, **49**, 632–637.
- 84 D. Chen, D. Yang, C. A. Dougherty, W. Lu, H. Wu, X. He, T. Cai, M. E. Van Dort, B. D. Ross and H. Hong, *ACS Nano*, 2017, **11**, 4315–4327.
- 85 D. Zhao, W. Zhang, Z.-H. Wu and H. Xu, *Front. Chem.*, 2022, **9**.
- 86 J. Park, Q. Jiang, D. Feng and H.-C. Zhou, *Angew. Chem., Int. Ed.*, 2016, **55**, 7188–7193.
- 87 R. Riccò, W. Liang, S. Li, J. J. Gassensmith, F. Caruso, C. Doonan and P. Falcaro, *ACS Nano*, 2018, **12**, 13–23.
- 88 H. Wang, J. J. Mahle, T. M. Tovar, G. W. Peterson, M. G. Hall, J. B. DeCoste, J. H. Buchanan and C. J. Karwacki, *ACS Appl. Mater. Interfaces*, 2019, **11**, 21109–21116.
- 89 S. J. Garibay, O. K. Farha and J. B. DeCoste, *Chem. Commun.*, 2019, **55**, 7005–7008.
- 90 Z. Chen, T. Islamoglu and O. K. Farha, *ACS Appl. Nano Mater.*, 2019, **2**, 1005–1008.
- 91 S. Y. Moon, E. Prousaloglou, G. W. Peterson, J. B. DeCoste, M. G. Hall, A. J. Howarth, J. T. Hupp and O. K. Farha, *Chemistry*, 2016, **22**, 14864–14868.
- 92 K. Y. Cho, J. Y. Seo, H.-J. Kim, S. J. Pai, X. H. Do, H. G. Yoon, S. S. Hwang, S. S. Han and K.-Y. Baek, *Appl. Catal., B*, 2019, **245**, 635–647.
- 93 T. Islamoglu, M. A. Ortuño, E. Prousaloglou, A. J. Howarth, N. A. Vermeulen, A. Atilgan, A. M. Asiri, C. J. Cramer and O. K. Farha, *Angew. Chem., Int. Ed.*, 2018, **57**, 1949–1953.
- 94 H. J. Park, J. K. Jang, S. Y. Kim, J. W. Ha, D. Moon, I. N. Kang, Y. S. Bae, S. Kim and D. H. Hwang, *Inorg. Chem.*, 2017, **56**, 12098–12101.
- 95 M. C. de Koning, M. van Grol and T. Breijaert, *Inorg. Chem.*, 2017, **56**, 11804–11809.
- 96 Y. Zhang, X. Zhang, J. Lyu, K. I. Otake, X. Wang, L. R. Redfern, C. D. Malliakas, Z. Li, T. Islamoglu, B. Wang and O. K. Farha, *J. Am. Chem. Soc.*, 2018, **140**, 11179–11183.